# CHAPTER IV
# RESULTS AND DISCUSSION

## 4.1 Nickel Ferrite Synthesis

### 4.1.1 EDX and SEM Results

Three different regions of the synthesized nickel ferrite were examined with EDX for weight percent of iron and nickel oxide. It should be noted that this analysis cannot distinguish between $Fe^{2+}$ and $Fe^{3+}$, resulting in the total weight percentage less than a hundred. From Table 4.1, the average molecular composition of iron and nickel in nickel ferrite was found to be 2.28 and 0.72, respectively. Hence, the synthesized nickel ferrite was $Ni_{0.72}Fe_{2.28}O_4$. The calculation of nickel ferrite composition is given in Appendix A.

Scanning electron microscopy with two different magnifications showed the microstructure of nickel ferrite in Figures 4.1 and 4.2. The SEM analysis showed that the average size of the nickel ferrite particles varies between 1-2 μm.

**Table 4.1** EDX analysis of nickel ferrite

| Average weight % | |
|---|---|
| FeO | NiO |
| 67.62 | 22.15 |

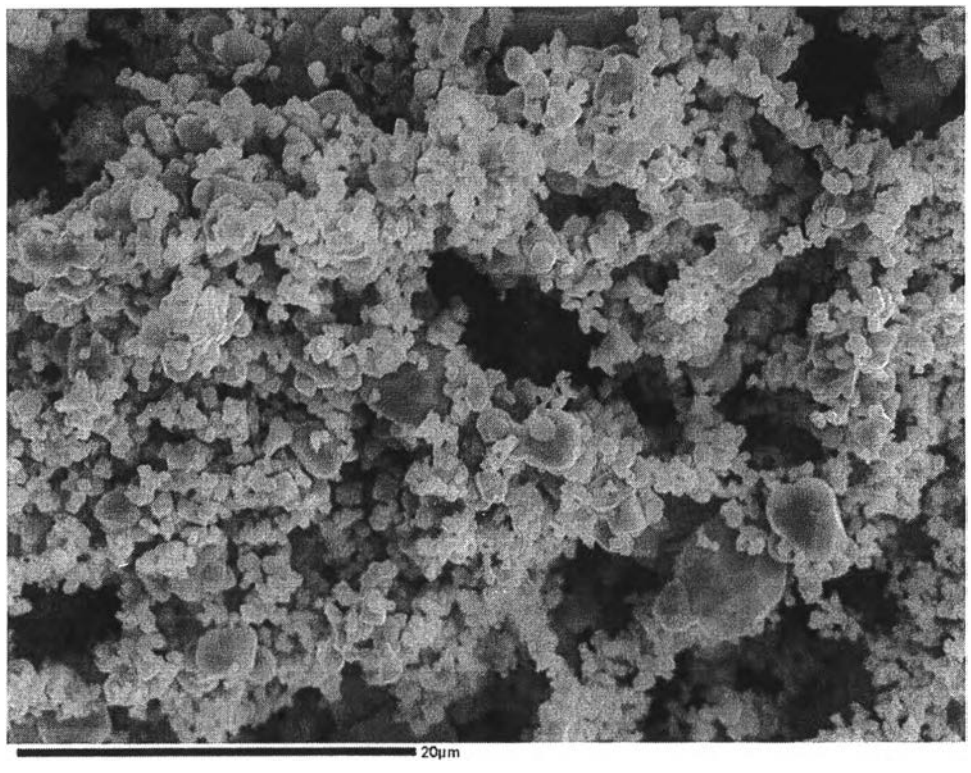


**Figure 4.1** Scanning electron micrograph of $Ni_{0.72}Fe_{2.28}O_4$ at 2,500 magnification.

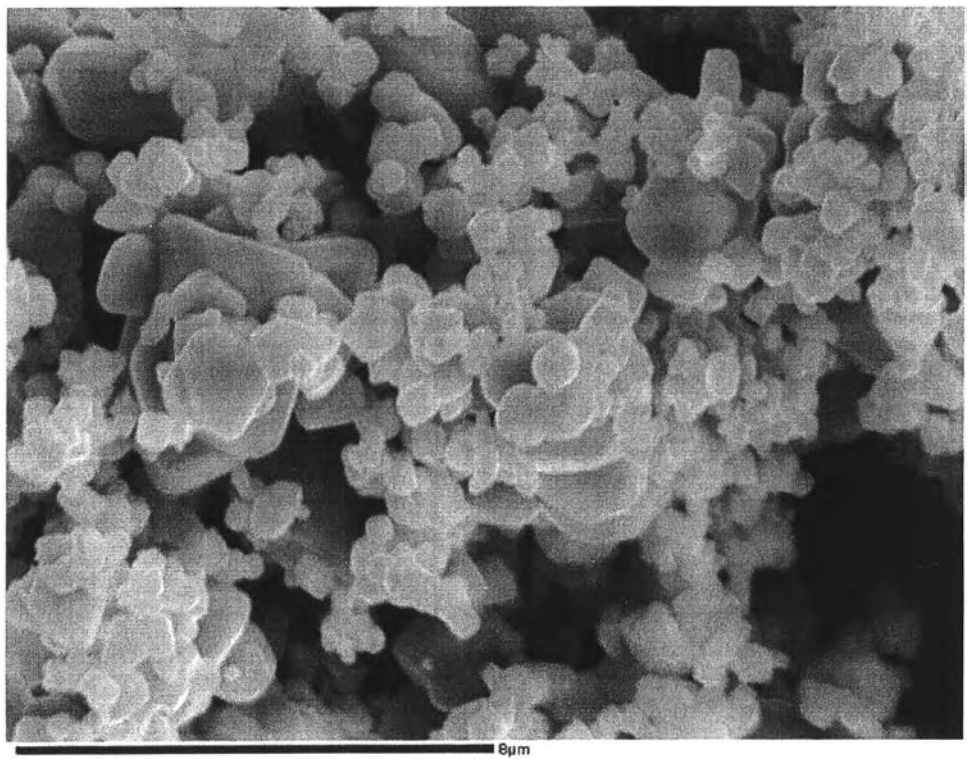


**Figure 4.2** Scanning electron micrograph of $Ni_{0.72}Fe_{2.28}O_4$ at 7,500 magnification.

4.1.2 XRD Results

Figure 4.3 shows the XRD pattern of synthesized non-stoichiometric nickel ferrite. It should be noted that the XRD patterns of both magnetite and nickel ferrite are about the same since their structures are inverse spinel (Deer *et al.*, 1985). The difference is the minor variation in the 2θ values which, in turn, give different lattice parameters, $a_0$. The lattice parameter was calculated from d-spacing values by using the formula

$$a_0 = d\sqrt{h^2 + k^2 + l^2} \tag{4.1}$$

and from calculation the lattice parameter of $Ni_{0.72}Fe_{2.28}O_4$ was 8.349 Å. Details of the calculation are given in Appendix B.

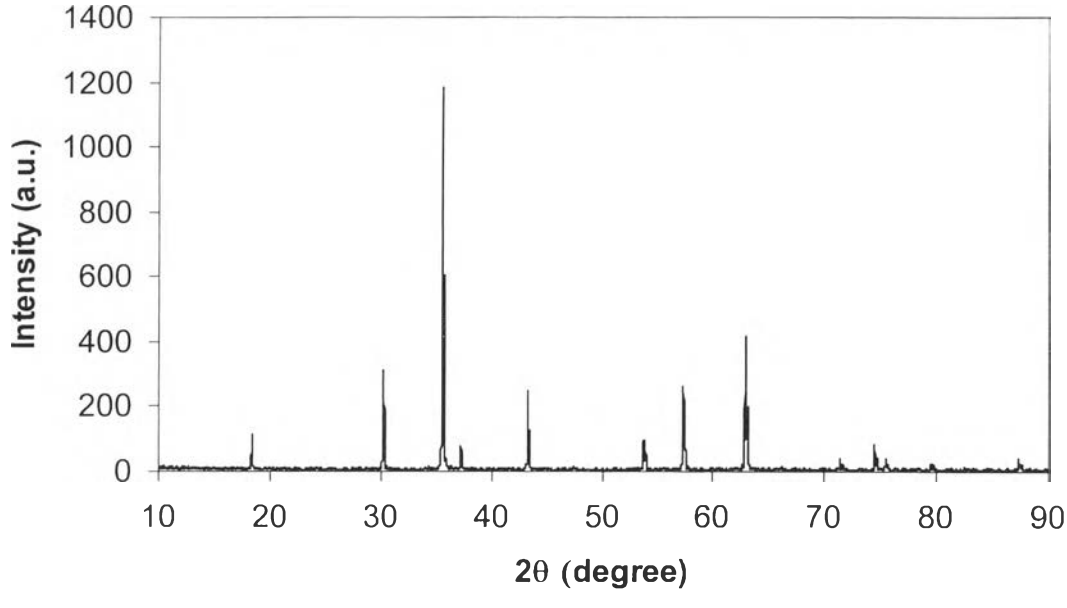


**Figure 4.3** XRD pattern of nickel ferrite.

In order to distinguish nickel ferrite from magnetite, Vegard's relationship was applied. Vegard's law is an empirical relationship between lattice parameter of a three-dimensional solid solution and its composition. Therefore, a lattice parameter of non-stoichiometric nickel ferrite, $Ni_xFe_{3-x}O_4$, must be in-between those of magnetite, $Fe_3O_4$, and stoichiometric nickel ferrite, $NiFe_2O_4$. Lattice

parameter values of magnetite, non-stoichiometric nickel ferrite and stoichiometric nickel ferrite were tabulated in Table 4.3, and plotted in Figure 4.4.

**Table 4.2** Comparison of lattice parameters

| Substances | Lattice parameter (Å) |
|---|---|
| $Fe_3O_4$ | 8.396* |
| $Ni_{0.72}Fe_{2.28}O_4$ | 8.349 |
| $NiFe_3O_4$ | 8.339* |

*From Powder Diffraction File (PDF), International Centre for Diffraction Data.

Vegard's law was successfully applied to the nickel ferrite solid solution as observed by Ranganathan (2001). It also agreed well with this experiment. Hence, the results from EDX and XRD confirmed that the synthesized nickel ferrite is of the composition of $Ni_{0.72}Fe_{2.28}O_4$.

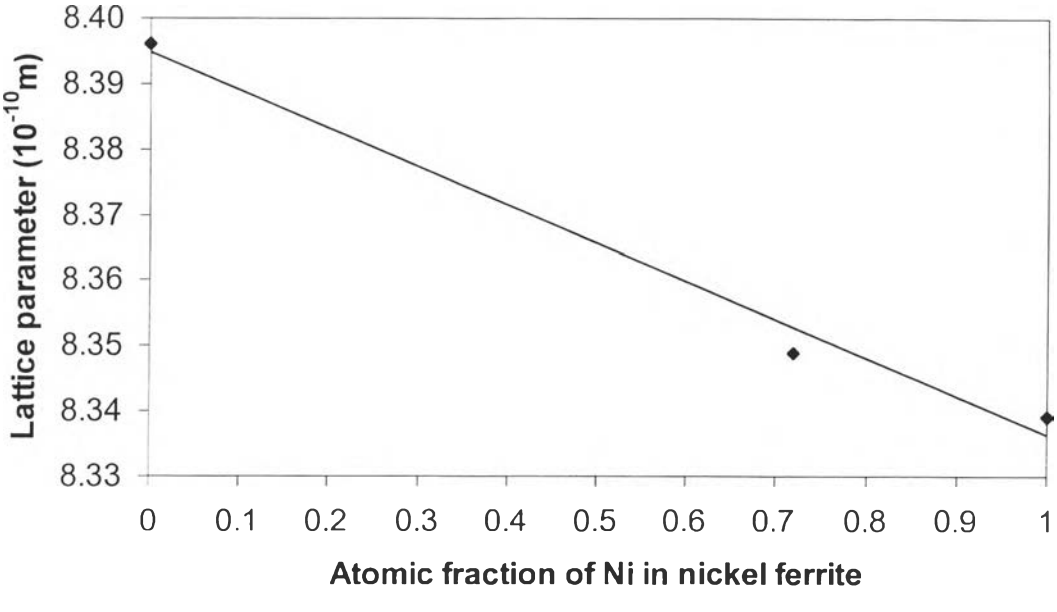


**Figure 4.4** Variation of lattice parameters with composition x in $Ni_xFe_{3-x}O_4$.

## 4.2 Nickel Ferrite Deposition

### 4.2.1 Effect of Surface Boiling

The amount of the deposit on the top coupons was significantly higher than that on the bottom coupons; the differences could be distinguished with the naked eye. The values were given in Tables 4.3 to 4.5. The Scanning Electron Microscope (SEM) revealed the surface morphology of the top and the bottom coupons of three experiments at different magnifications, as depicted in Figures 4.5 to 4.16. The deposit morphology indicated "chimneys", typical of wick boiling, covering the whole surface of the top coupons. The sizes of chimneys were about 20-25 μm. Only clumps of deposits were observed on the bottom coupons. It can be explained, as reported by Basset (1999), and Kondratova and Lister (2000), that the deposition was controlled by microlayer evaporation and by the process of bubble nucleation and bubble growth at preferred sites on the heated surfaces. Such sites remained crud-free, but mass transfer of particles around the sites was increased, resulting in particle deposition and chimneys later on. Since the surface temperature of the bottom coupons was lower than that of the top coupon, and there was no boiling on the bottom coupons according to the surface morphology, the deposits were significantly less. Particle sizes of deposits were about 1-2 μm, similar to those of synthesized nickel ferrite.

The deposit composition analyzed with Energy Dispersive X-ray (EDX) was tabulated is Table 4.3. For the top coupon, three spots were randomly selected and averaged since the deposits covered the whole surface. Percentages of iron and nickel oxide in the deposits were similar to those of synthesized nickel ferrite. According to the particle size and the composition, then, the deposits were predominantly injected nickel ferrite.

For the bottom coupon, zirconium contributed considerably to the analysis. This was due to the fact that zirconium was underneath the deposits, and on the bottom coupon the deposits were fairly thin. The electron beam was therefore able to generate a signal in the zirconium alloy substrate. It should be noted that some oxide contents are given as ranges because the values obtained were different from the average values by more than 2%. Iron oxide content was decreased to

about 50% by weight. It is unlikely that the $ZrO_2$ contribution is responsible for this effect because only iron oxide content decreased; nickel oxide content remained almost the same. According to Sandler and Kunig (1981), the solubility of iron and nickel from $Ni_{0.6}Fe_{2.4}O_4$ at $pH_{300°C}$ 5 decreased with increasing temperature, and the solubility of iron was higher than that of nickel by a factor of four. It should be kept in mind that the ratio of iron and nickel concentrations in the solid is about four. Since the temperature of the top coupons was higher than that of the bottom coupons, it is likely that iron and nickel would dissolve more on the bottom coupons. No boron was observed in any of the analyses.

The coupons with their deposits were analyzed with XRD to ensure the presence of nickel ferrite. The XRD patterns of the top and the bottom coupons from Run1 are shown in Figures 4.17 and 4.18, respectively. Zirconium peaks from the substrate underneath the deposits were present. A bare zirconium surface was also analyzed to identify zirconium peaks, and its XRD pattern is given in Appendix C. The arrows in Figure 4.17 point at the peaks which correspond to nickel ferrite. Therefore, it can be confirmed that the injected nickel ferrite deposited on the surfaces. It is unlikely that nickel ferrite peaks can be seen in analyses of the bottom coupon because the amount of the deposits was so small. The XRD results from Run2 and Run3 also showed the nickel ferrite pattern only on the top coupons.

**Table 4.3** EDX analysis of the deposits

| Run | Coupon | Weight % | | | |
|---|---|---|---|---|---|
| | | FeO | NiO | $ZrO_2$ | ZnO |
| 1 | Top | 66.22 | 21.99 | - | - |
| 1 | Bottom | 49-57 | 18-22 | 14-25 | - |
| 2 | Top | 66.90 | 22.36 | - | - |
| 2 | Bottom | 46-53 | 19-24 | 9-22 | - |
| 3 | Top | 66.85 | 23.61 | 0.29 | - |
| 3 | Bottom | 52.33 | 21.62 | 11-14 | 1.13 |

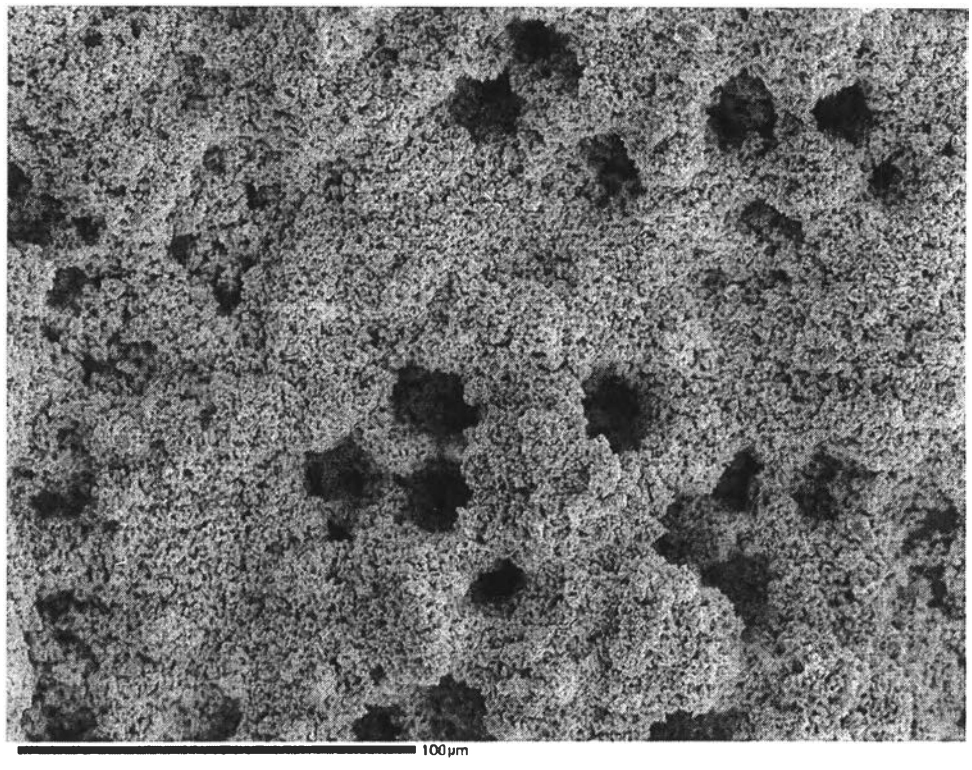


**Figure 4.5** Deposits on the top coupon, Run1 at 500 magnification.

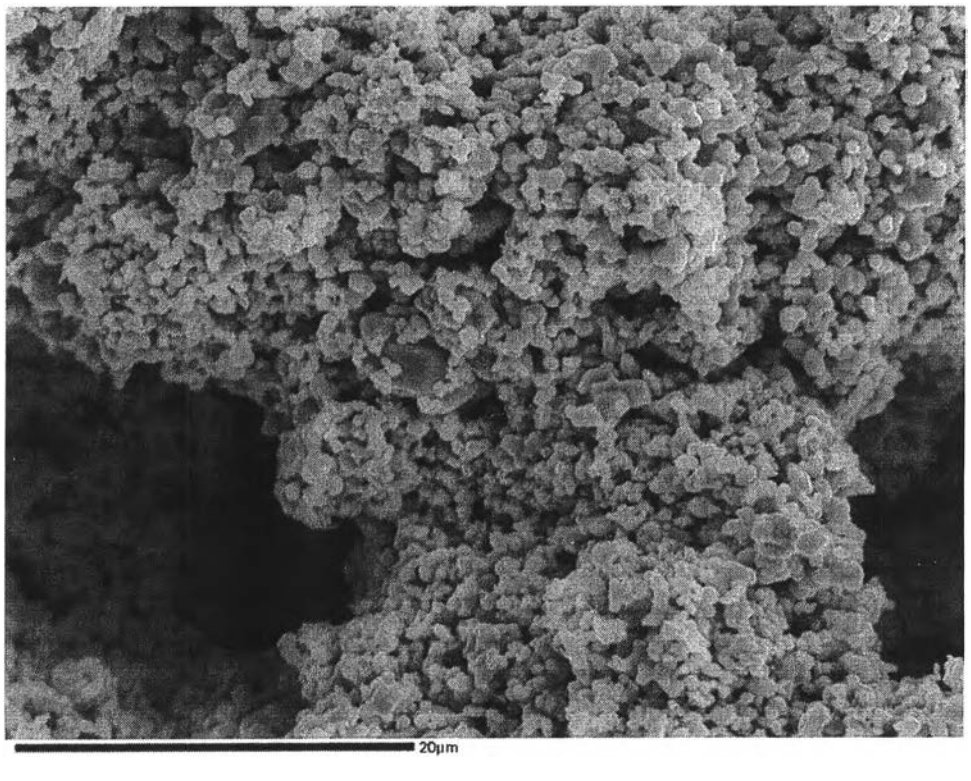


**Figure 4.6** Deposits on the top coupon, Run1 at 2,500 magnification.

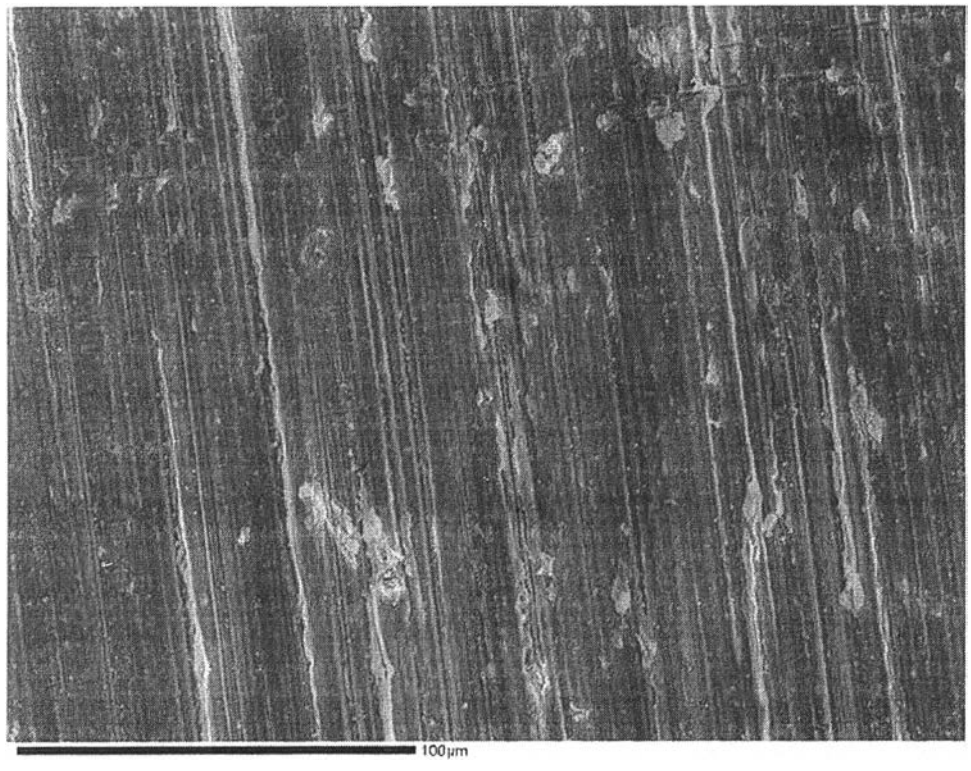


**Figure 4.7** Deposits on the bottom coupon, Run1 at 500 magnification.

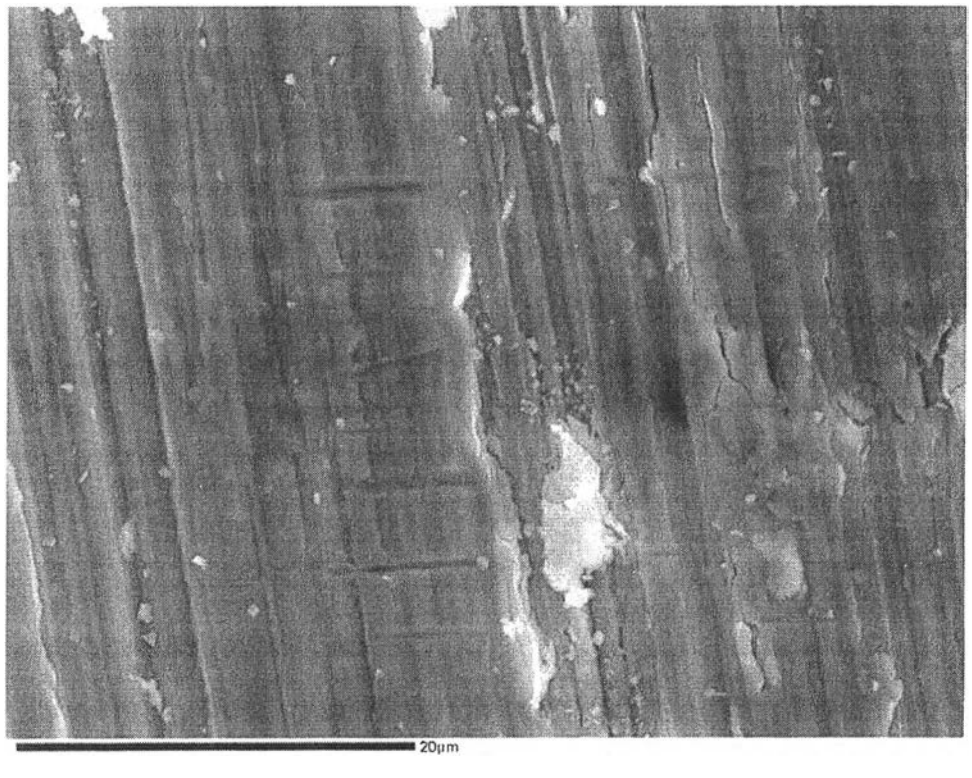


**Figure 4.8** Deposits on the bottom coupon, Run1 at 2,500 magnification.

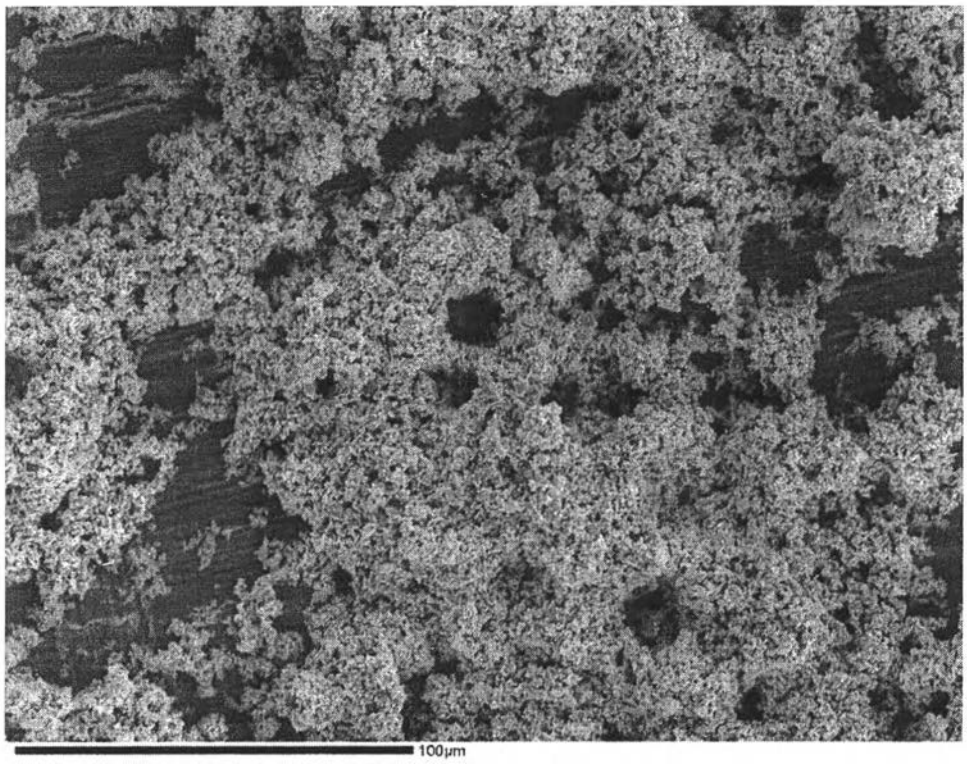


**Figure 4.9** Deposits on the top coupon, Run2 at 500 magnification.

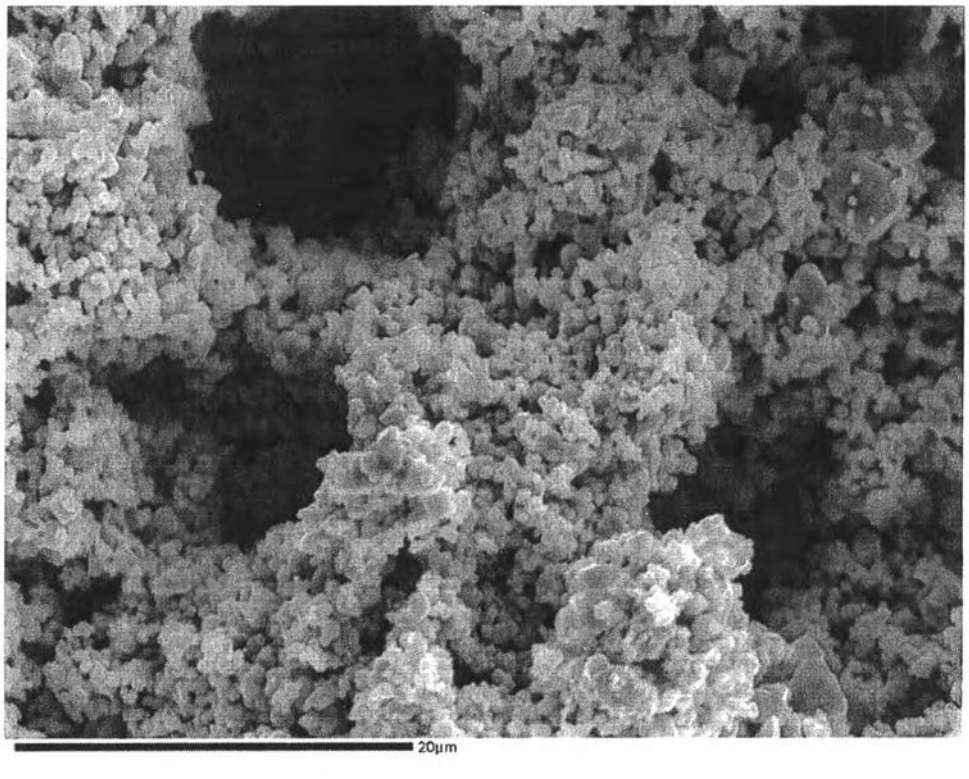


**Figure 4.10** Deposits on the top coupon, Run2 at 2,500 magnification.


**Figure 4.11** Deposits on the bottom coupon, Run2 at 500 magnification.

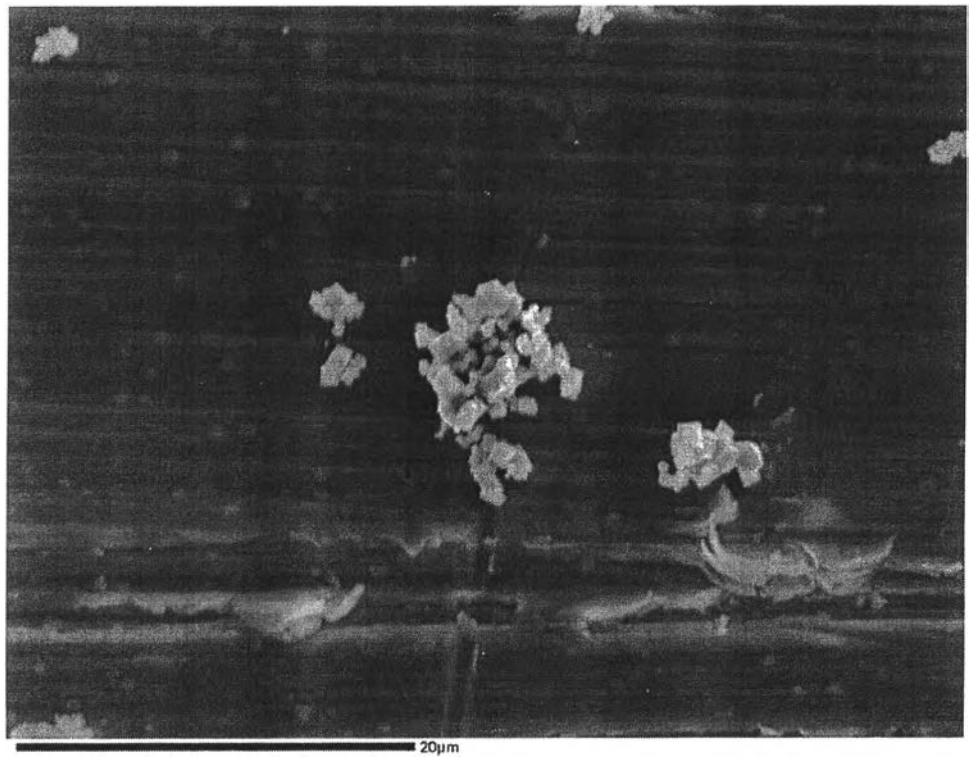


**Figure 4.12** Deposits on the bottom coupon, Run2 at 2,500 magnification.

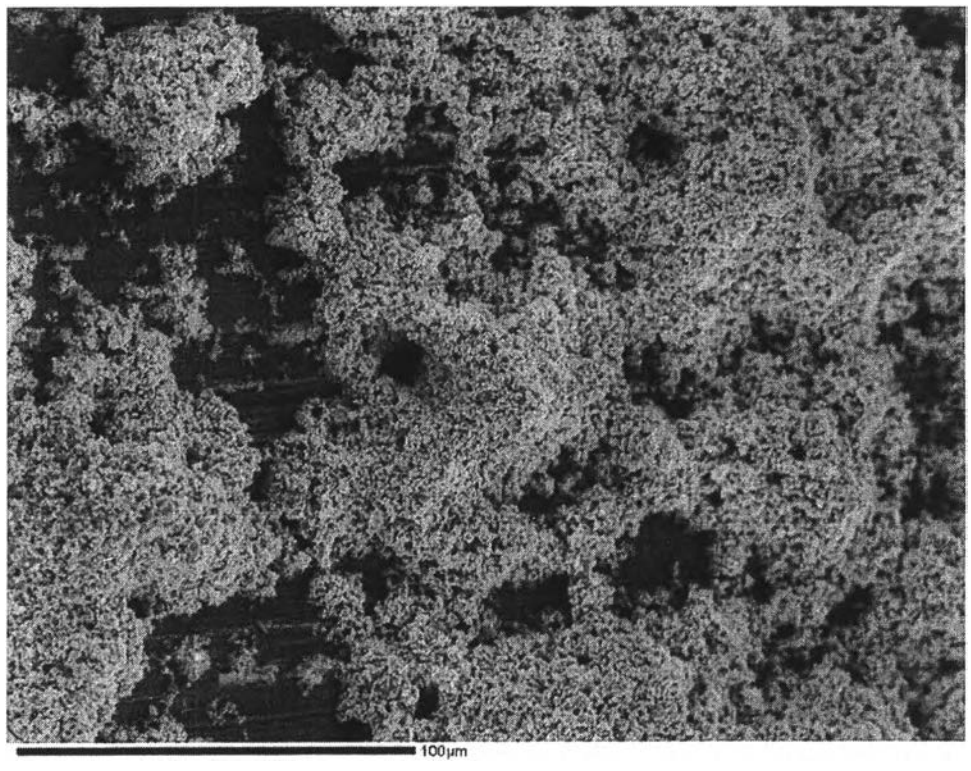


**Figure 4.13** Deposits on the top coupon, Run3 at 500 magnification.

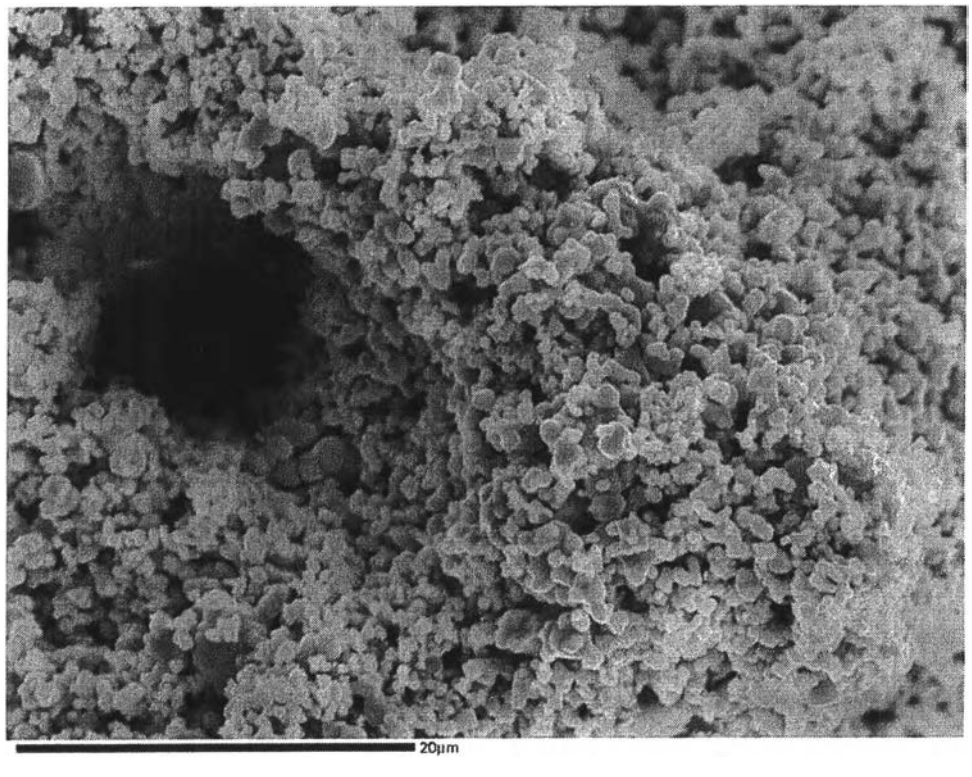


**Figure 4.14** Deposits on the top coupon, Run3 at 2,500 magnification.

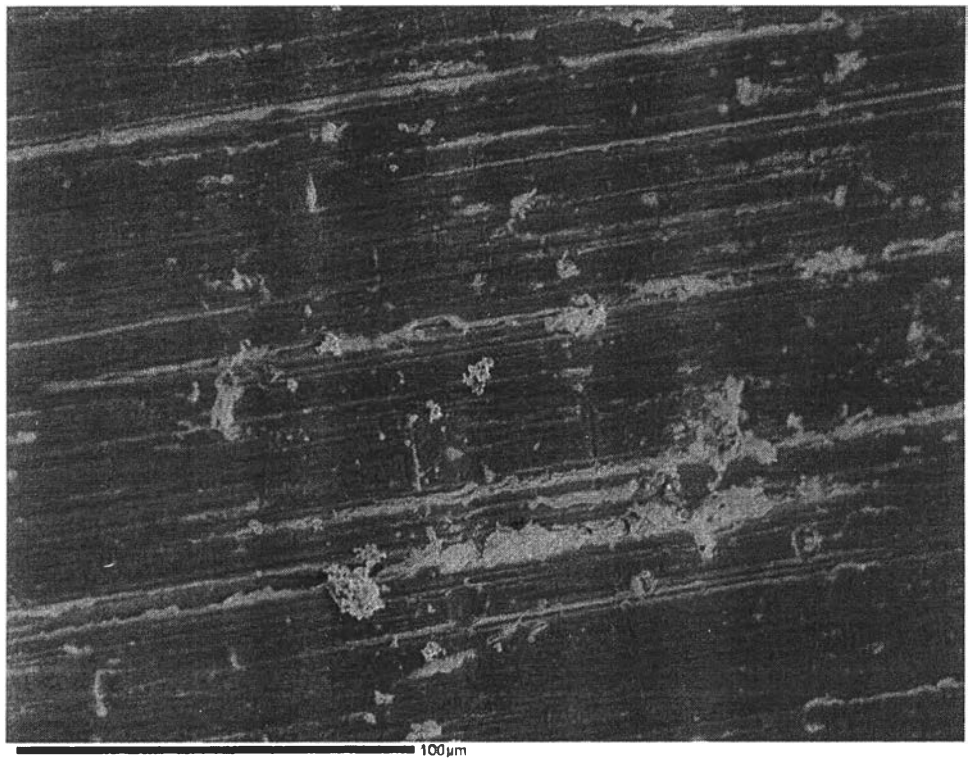


**Figure 4.15** Deposits on the bottom coupon, Run3 at 500 magnification.

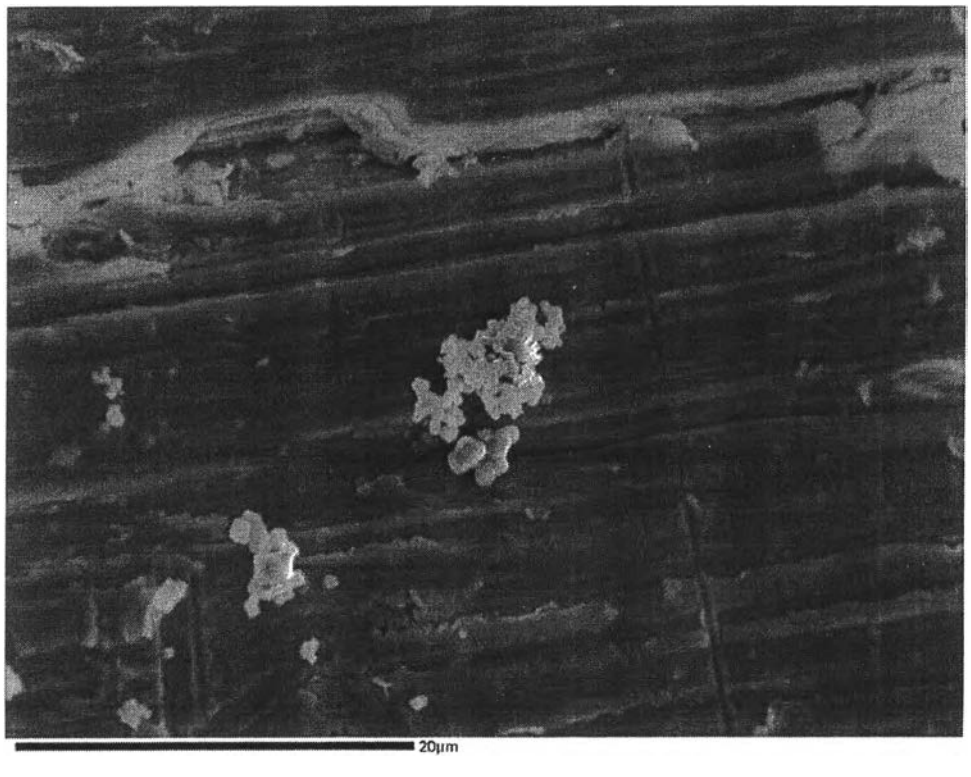


**Figure 4.16** Deposits on the bottom coupon, Run3 at 2,500 magnification.

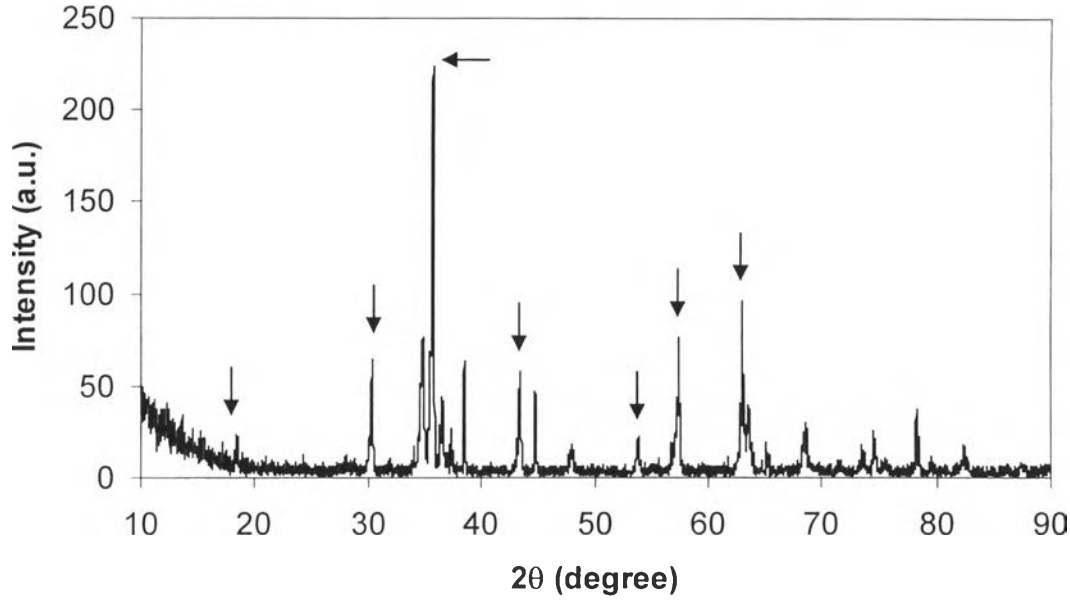


**Figure 4.17** The XRD pattern of the top coupon, Run1; arrows indicate nickel ferrite peaks

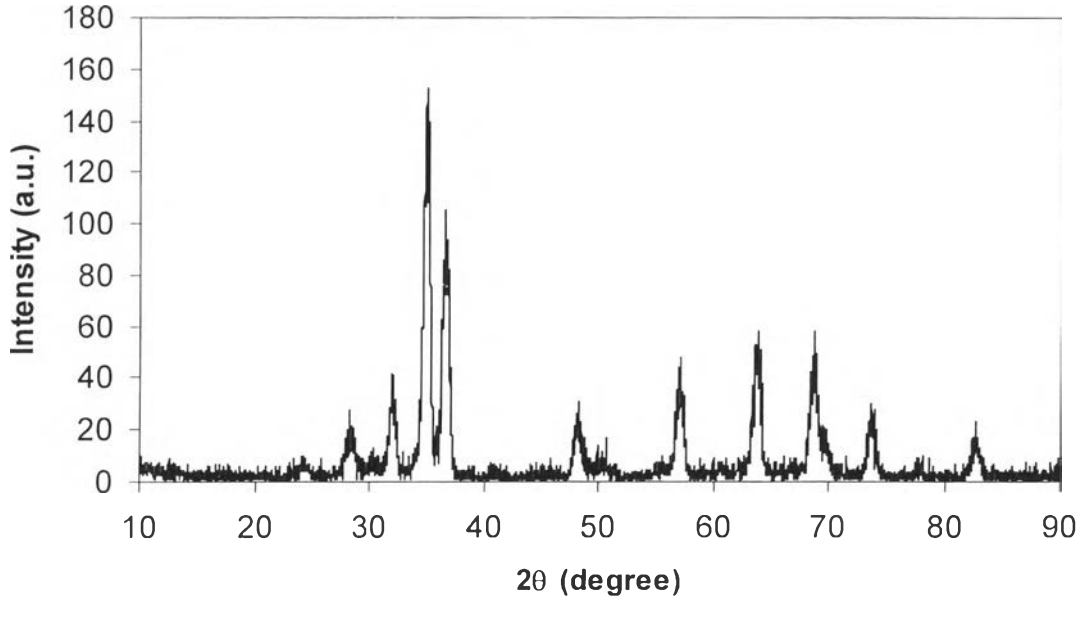


**Figure 4.18** The XRD pattern of the bottom coupon, Run1.

4.2.2 Effect of pH

There were more deposits on the heated surface in the lower pH condition. The amounts of deposit in Run1 and Run2 are given in Table 4.4. This can be explained by the fact that pH induces changes in the surface charge of nickel ferrite particles and zirconium oxide surfaces. Mathur and Venkataramani (1998) reported PZC of magnetite substituted with nickel; the PZC of $Ni_{0.72}Fe_{2.28}O_4$ was found to be 6.0. The PZC of zirconium was in the range of 6.0-6.5, as reported by Regazzoni *et al.* (1983). This suggests that at pH 6.8 the interaction force between the nickel ferrite particles and the zirconium oxide surface was less repulsive than at pH 7.0. It should be kept in mind, however, that the duration of Run2 was 10 hours less than that of Run1.

The effect of pH was much clearer on the top coupon, indicating that there was a synergistic effect of pH and surface boiling. The deposit thickness was estimated by assuming a crud density of 2 $g/cm^3$ (estimated by plant experience – Westinghouse, 2000), and for the top coupon at $pH_{300°C}$ 6.8, the deposit thickness was found to be about 10 μm. On the bottom coupons, the deposits did not cover the whole surfaces. Nevertheless, deposit thicknesses were quoted.

**Table 4.4** Effect of pH

| Run | 1 | 2 | 1 | 2 |
|---|---|---|---|---|
| pH @300°C | 6.8 | 7.0 | 6.8 | 7.0 |
| Coupon | Top | Top | Bottom | Bottom |
| Amount of Fe ($mg/cm^2$) | 1.018 | 0.130 | 0.098 | 0.031 |
| Amount of Ni ($mg/cm^2$) | 0.376 | 0.049 | 0.035 | 0.011 |
| Deposit thickness (μm) | 9.86 | 1.28 | 0.93 | 0.30 |
| Deposition velocity (cm/h) | 28.17 | 3.93 | 2.67 | 0.92 |
| Weight % | | | | |
| FeO | 66.22 | 66.90 | 49-57 | 46-53 |
| NiO | 21.99 | 22.36 | 18-22 | 19-24 |
| $ZrO_2$ | - | - | 14-25 | 9-22 |

The total weight percentage of the oxides was less than a hundred since there were $Fe^{2+}$ and $Fe^{3+}$ contributed in the deposit, and the EDX analysis cannot distinguish.

4.2.3 Effect of Zinc Addition

Zinc addition to give 10 ppb in the coolant has an effect on the amount of the deposits, as shown in Table 4.5. With zinc addition, the amount of iron and nickel was increased less than a factor of two. This agreed with the investigation by Walters *et al.* (2002). In addition, as reported by Turnage (2004), more crud coverage was observed over the fuel assembly surfaces with zinc addition. However, most of those crud layers were relatively thin and had no effect of the fuel performance. It should be noted that in this work the crud concentration was extremely high, compare to the plant conditions. Therefore, crud concentration might swamp over zinc, and thus, the effect of zinc cannot be seen. No change in pH was observed during the experiment with zinc addition.

**Table 4.5** Effect of zinc addition

| Run | 2 | 3 | 2 | 3 |
|---|---|---|---|---|
| Zinc concentration (ppb) | - | 10 | - | 10 |
| Coupon | Top | Top | Bottom | Bottom |
| Amount of Fe ($mg/cm^2$) | 0.130 | 0.195 | 0.031 | 0.047 |
| Amount of Ni ($mg/cm^2$) | 0.049 | 0.081 | 0.011 | 0.012 |
| Amount of Zn ($mg/cm^2$) | - | 0.003 | - | 0.001 |
| Deposit thickness (μm) | 1.28 | 2.02 | 0.30 | 0.38 |
| Deposition velocity (cm/h) | 3.93 | 6.20 | 0.92 | 1.17 |
| Weight % | | | | |
| FeO | 66.90 | 66.85 | 46-53 | 52.33 |
| NiO | 22.36 | 23.61 | 19-24 | 21.62 |
| $ZrO_2$ | - | 0.29 | 9-22 | 11-14 |
| ZnO | - | - | - | 1.13 |

Zinc content associated with the deposits was found to be very small. It was reported by Beverskog (2004) that nickel ferrite is more stable than franklinite ($ZnFe_2O_4$). Zinc does not form a new solid phase but is incorporated into the crystal structure mostly as interstitials.

### 4.2.4 Boron Hideout Return

Sampling was undertaken after autoclave isolation to observe the change in boron concentration which, in turn, corresponded to boron hideout return. In Figures 4.19 and 4.20 are plotted the boron concentration and the autoclave temperature versus time from Run1 and Run3, respectively. It was found that there were slight increases in boron concentration in both cases. The maximum concentration differences were in the range of 90 and 60 ppm in Run1 and Run3, respectively, and were relatively small compare to the bulk concentration. It should be also noted that during the sampling the autoclave should be in saturated condition. Therefore, the changes in boron concentration can be contributed to the boron hideout return or the effect of water evaporation during the sampling or both. The changes in boron concentration due to water evaporation were calculated (see Appendix F) and plotted in Figures 4.19 and 4.20 for comparison. According to the measured and the calculated boron concentrations, water evaporation did not have a significant effect on the changes in boron concentration. Hence, these changes should be contributed to the boron hideout return. Amounts of boron hideout correspond to the changes in boron concentration in Run1 and Run3 were estimated to be 0.69 and 0.6 $mgB/cm^2$, respectively.

### 4.2.5 Other Observations: Particles from Filter

After the end of each run, particles from the loop filter were analyzed for the composition as tabulated in Table 4.6. Some values in the table are given in ranges because the initial values were more than 2% different from the average values. The iron content in the particles decreased, while the nickel content remained almost the same with respect to the synthesized nickel ferrite. This may be due to the fact, as discussed earlier, that iron solubility in nickel ferrite is higher than that of nickel (Sandler and Kunig, 1981). Particle sizes, as depicted in Figure 4.21,

in all experiments were in the range of 1-2 μm, similar to those f the synthesized nickel ferrite.

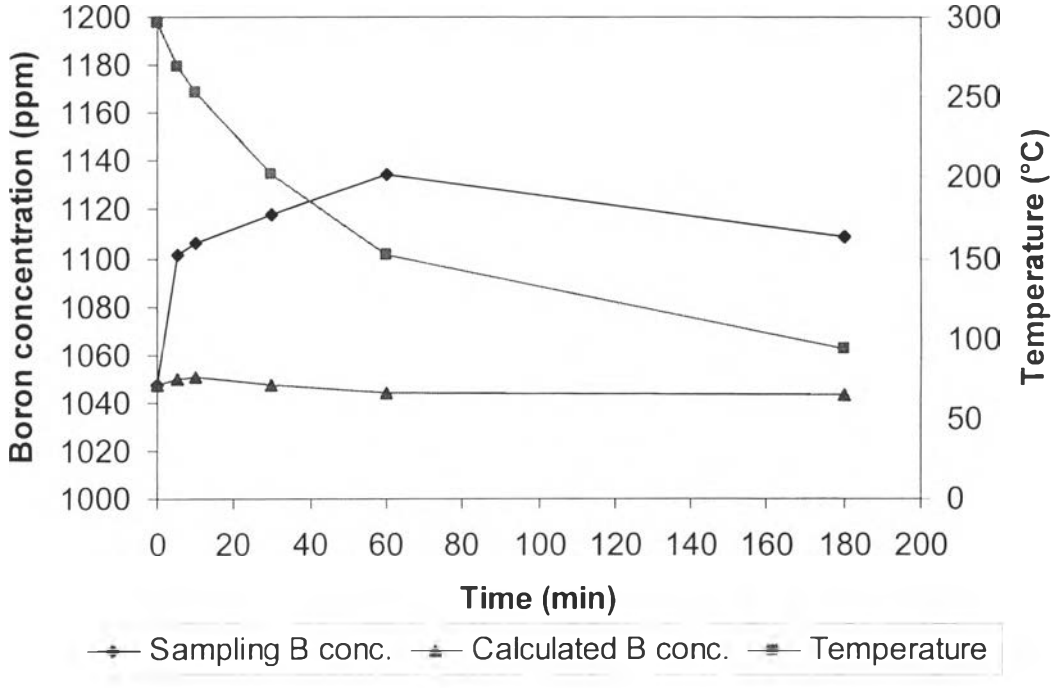


**Figure 4.19** Boron hideout return and calculated boron concentration from Run1.

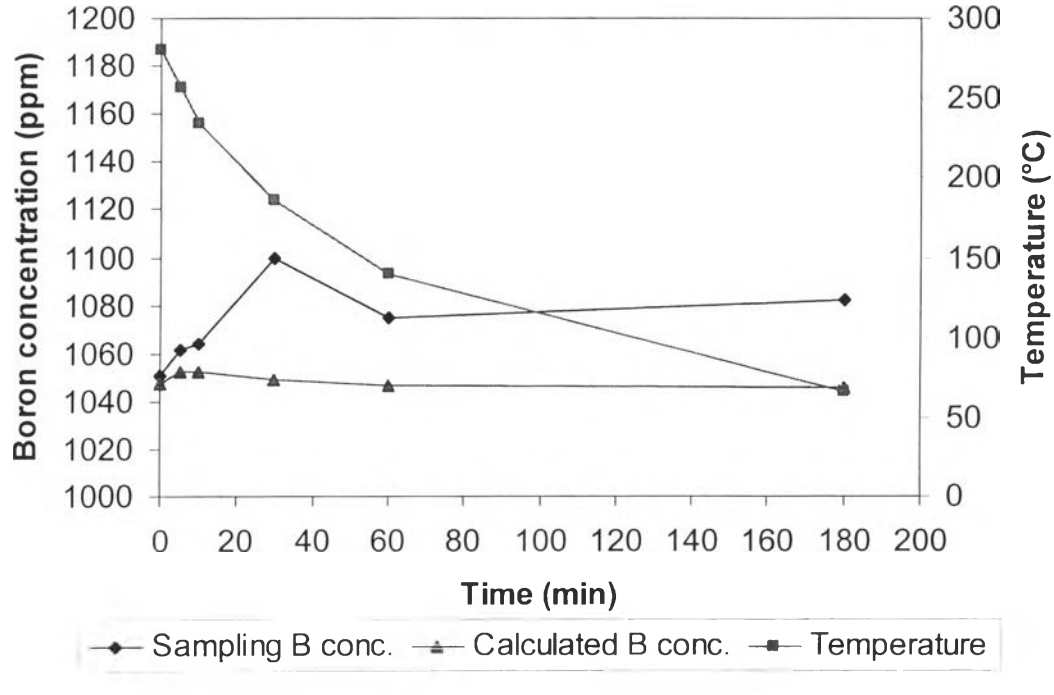


**Figure 4.20** Boron hideout return and calculated boron concentration from Run3.

**Table 4.6** EDX analysis of particles from the filter

| Run | Weight % | | |
|---|---|---|---|
| | FeO | NiO | ZnO |
| 1 | 55-61 | 20-23 | - |
| 2 | 65.13 | 24.27 | - |
| 3 | 61-65 | 23.6 | 0.34 |

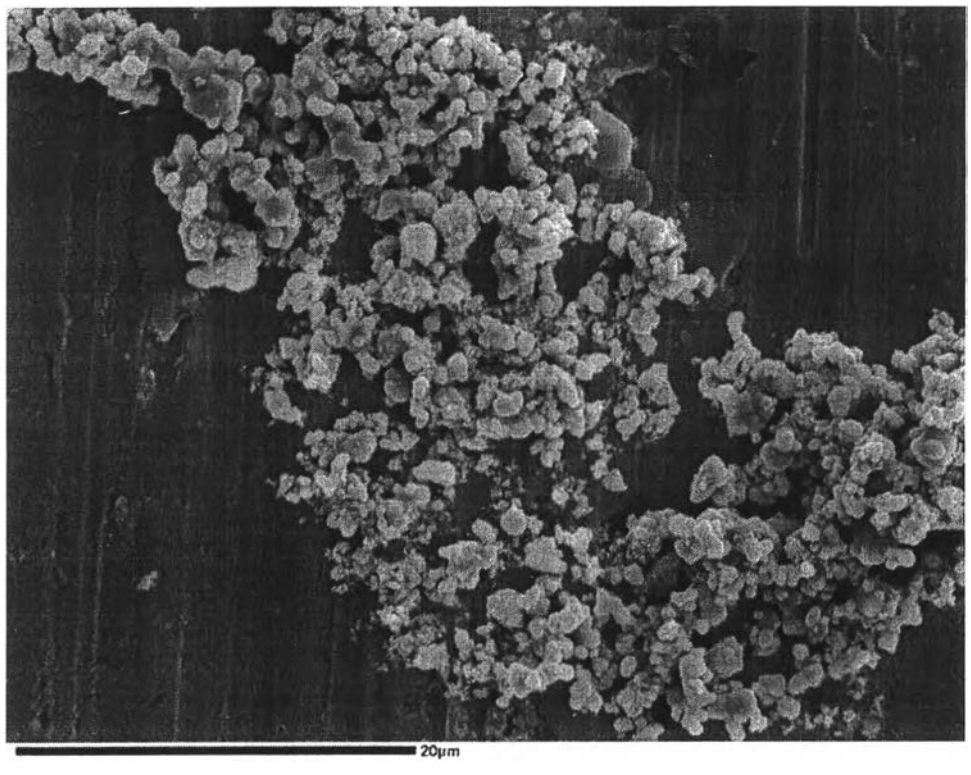


**Figure 4.21** Particles from the filter, Run2.

4.2.6 Other Observations: Autoclave Upstream and Downstream Sampling

Autoclave upstream and downstream sampling (i.e. sampling from the bottom of the autoclave and from the autoclave outlet, as indicated in Figure 3.2) was undertaken during the experiments to observe any differences in nickel ferrite and zinc concentration caused by deposition. Nickel ferrite was injected to obtain the nominal concentration of 500 ppb, which corresponds to iron and nickel concentrations of 270 and 90 ppb, respectively. Sampling values for Run1, 2 and 3

are given in Figures 4.22, 4.23, and 4.24, respectively. Data for nickel concentration in Run3 are not available because there was an error during the sample preparation.

The results showed that iron, nickel and zinc concentrations in all experiments fluctuated. It is believed to be the effect of sampling procedure. According to Figure 3.2, upstream and downstream samples had to be cooled down before being taken. With limited cooling capacity, samples can only be taken quite slowly; slower than the coolant velocity. Therefore, the sampling was not isokinetic and, in any case, the sample take-off tubes were not pointing into the flow direction. It is likely that the samples had fewer particles then the coolant. Furthermore, it is possible that particles would deposit in the sampling lines.

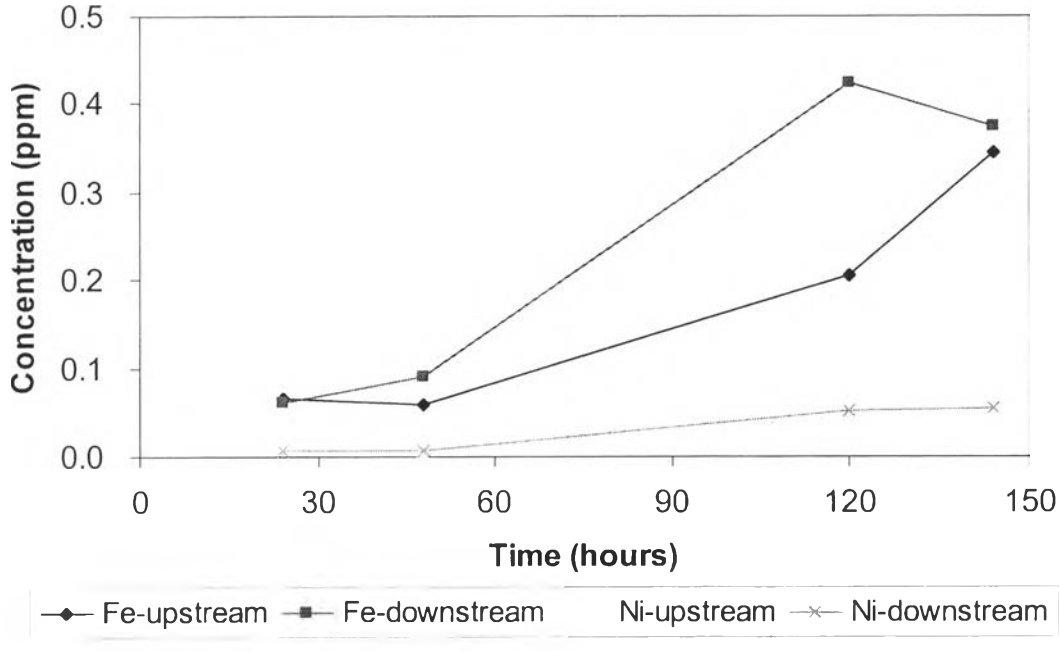


**Figure 4.22** Autoclave upstream and downstream sampling from Run1.

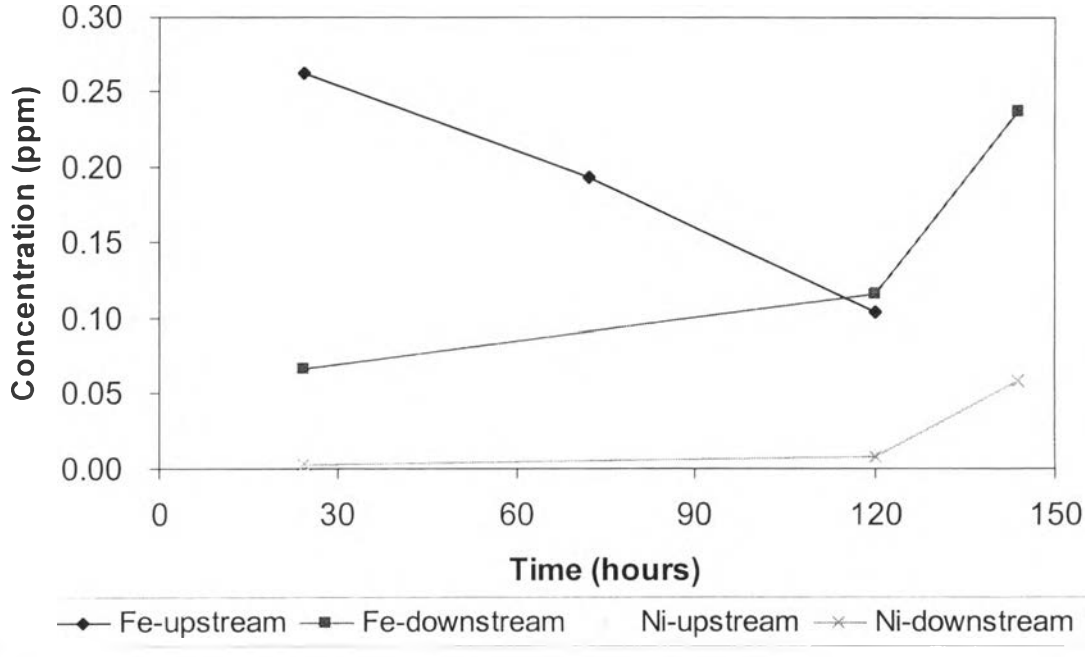


**Figure 4.23** Autoclave upstream and downstream sampling from Run2.

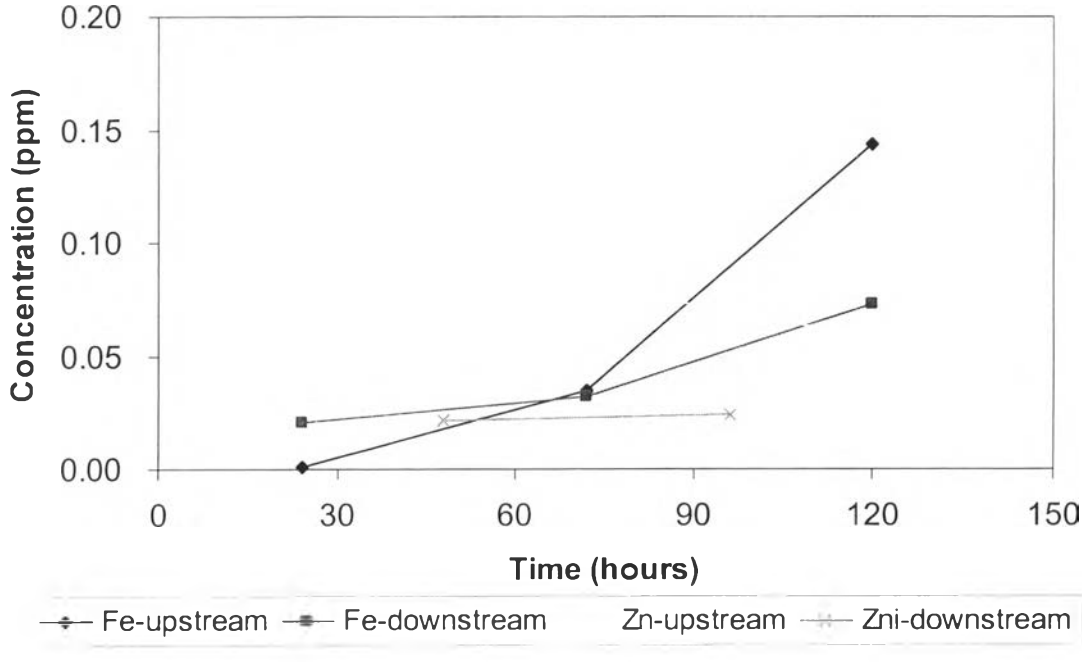


**Figure 4.24** Autoclave upstream and downstream sampling from Run3.

## 4.3 Boron Measurement with Neutron-Based Techniques

### 4.3.1 Neutron Slowing-Down Followed by Absorption

Counts were taken at Gain 50 and 100 to observe the effects of amplification on the stability of the data. Results from a one-minute counting period for ten measurements, for the central tube with and without boric acid powder, are tabulated in Table 4.7. It is obvious that the increase in amplification increases the number of counts. In the case of Gain 50, the standard deviations based on a Poisson distribution agreed with those of a normal distribution. On the other hand, the standard deviations in the case of Gain 100 were large and were totally different for the two distributions. It should be noted that Poisson statistics are commonly applied to radiation measurements, but standard deviations are based on the normal distribution (Knoll, 1989; Tsoulfanidis, 1995; and Hussein, 2003). It is believed that noise contributed to the fluctuation of counts. The higher the amplification, the more noise was generated in the counting.

In trying to identify the noise regime, the MCA was employed. A typical pulse-height distribution recorded by the MCA is shown in Figure 4.25. The channel number on the x-axis corresponds to the energy of the neutrons. The y-axis corresponds to the counts per channel. Since noise was amplified with amplification, a lower Gain of 20 was used. In Figure 4.25, three peaks are evident at different channels: 25, 100 and 560. The first peak was due to gamma rays, and some low energy neutrons. The second and the third peaks correspond to epithermal neutrons and full-energy neutrons from the Californium source, respectively (Hussein, 2003). It should be noted that low counts caused greater scatter of the data, since radiation is emitted from the radioisotopic source in a random fashion. Moreover, the result at Gain 20 showed that the MCA channels were not well utilized, since only about 800 channels were used out of the total of 2048 channels. In order to improve the quality and stability of the data and since all peaks were identified, a higher gain and longer counting period were employed. Once the amplification was increased, peaks were shifted to the right, and higher overall counts were obtained.

At Gain 50, the noise was high. A number of experiments were conducted, in which modifications were made, e.g. paraffin wax was placed in front

of the source and/or beside the autoclave. All results showed that the best discrimination between boron and no boron in each condition was found in the energy range between the tail of noise and the beginning of epithermal peak, as shown in Figure 4.26. No discrimination could be seen at the full-energy peak. This is consistent with the fact that the ability to absorb neutrons decreases with increasing neutron energy.

**Table 4.7** Counts in one minute obtained from counter with two different Gains

| | Without boric acid | | With boric acid | |
|---|---|---|---|---|
| #Measurement | Gain 50 | Gain 100 | Gain 50 | Gain 100 |
| 1 | 362 | 2201 | 408 | 3108 |
| 2 | 392 | 2344 | 357 | 3272 |
| 3 | 403 | 2979 | 375 | 3182 |
| 4 | 362 | 3368 | 384 | 2772 |
| 5 | 340 | 3253 | 376 | 2761 |
| 6 | 368 | 3436 | 353 | 2499 |
| 7 | 352 | 3744 | 377 | 1714 |
| 8 | 366 | 3491 | 395 | 1944 |
| 9 | 342 | 3510 | 361 | 1667 |
| 10 | 358 | 3337 | 390 | 1443 |
| Average | 364.5 | 3166.3 | 377.6 | 2436.2 |
| Standard deviation based on Poisson distribution | 19.09 | 56.27 | 19.43 | 49.36 |
| Standard deviation based on normal distribution | 19.92 | 511.04 | 17.44 | 688.82 |

Higher amplifications than Gain 50 were tried, but the MCA processing dead time became excessive. It should be kept in mind that increasing the Gain not only amplified the signal but also magnified the noise. Therefore, an amplification of Gain 50 was used for the rest of the experiments.

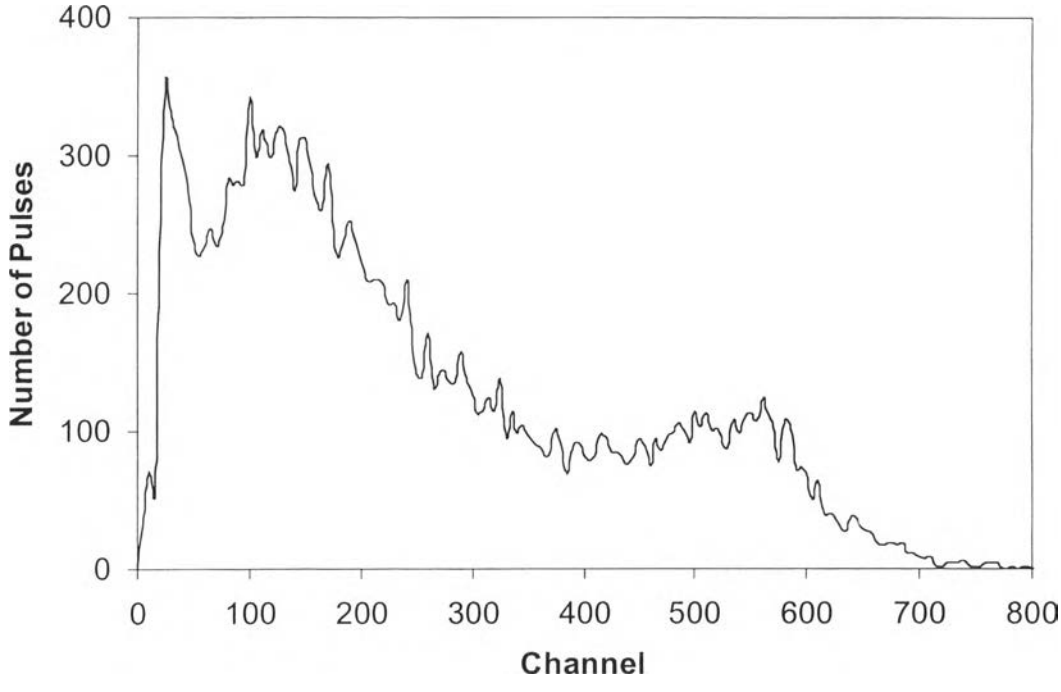


**Figure 4.25** Pulse-height distribution from the MCA; Gain 20 and 10-minute counting period.

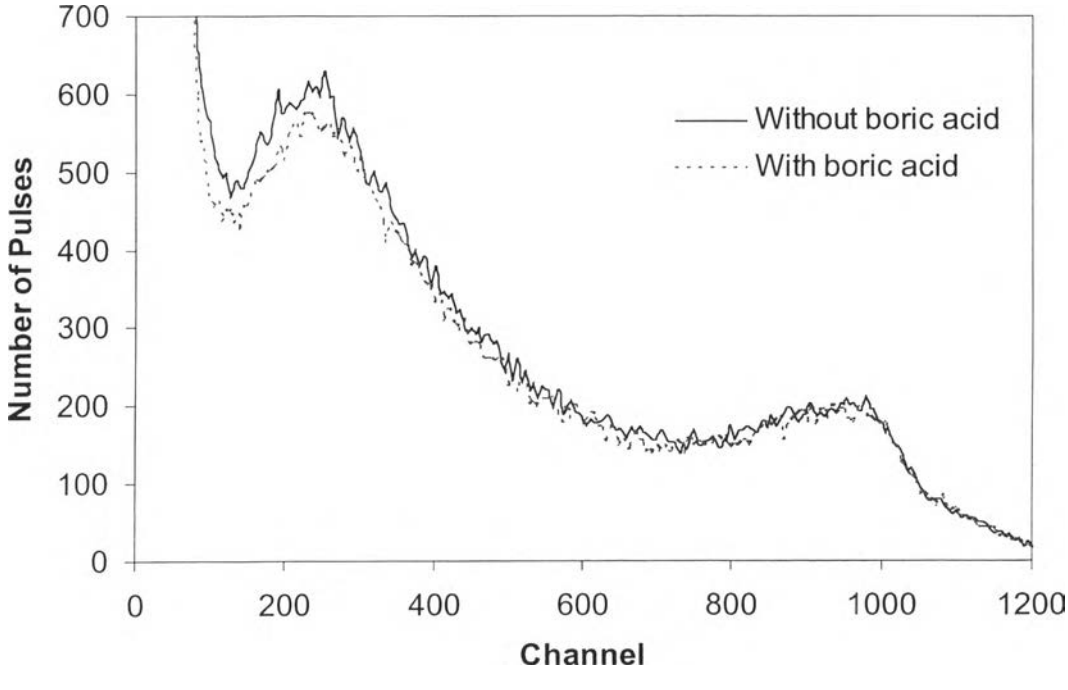


**Figure 4.26** Comparison of pulse-height distribution with and without boric acid; Gain 50 and 30-minute counting period.

Table 4.8 shows the maximum ratio of the counts without and with boric acid that can be obtained in each arrangement at Gain 50 with a 30-minute counting period. By placing paraffin wax in front of the source, besides and on top of the autoclave, the ratios of counts with and without boric acid were improved. On the other hand, too much wax in front of the autoclave reduced the ratio. Wax not only moderates the neutron energy but also reflects neutrons. Hence, wax placed besides and on top of the autoclave induced more thermal neutrons, which can be absorbed by boron. In this work, two different arrangements of wax besides the autoclave were tried. A better result was obtained when the wax covered only half of the autoclave, as depicted in Figure 3.9. It was because wax in such arrangement reflected neutrons and created a thermal-neutron cloud that could be absorbed by the boron in the tube. On the other hand, an extra coverage of wax, as depicted in Figure 3.8, reflected neutrons to the detector, but those neutrons could not be absorbed by the boron in the middle of the autoclave and so interfered with the counting. Hence, the setup with 15 mm of wax in front of the source, on top of the autoclave and side shielding covering only half of the autoclave was used to for further experiments with the SCA.

The scanning on the SCA was done by first fixing the energy of the lower window and varying the energy of the upper window. The first lower energy was chosen to give a low count rate, which meant that the signals from noise and from most of the gamma rays were eliminated. Figure 4.27 shows the overall scanning from 1 to 10 V. It confirmed that the contrast could be observed best in a narrow range close to the epithermal peak. Smaller steps in the range of 0.7 to 1.1 V were done, as shown in Figure 4.28.

The ratio obtained in Figure 4.28 was highest at the upper window energy about 0.9 V. Then the upper window energy was fixed at 0.9 V and the lower window energy was varied. Figure 4.29 shows that the best ratio was obtained at the lower window energy of 0.38 V. It should be noted that the error bars presented in the figures were calculated based on the radiation statistics; details are given in Appendix G. The ratio obtained from the MCA was consistent with that obtained from the SCA.

**Table 4.8** Maximum ratio of the counts with and without boric acid

| Run | Wax thickness in front of source (mm) | Top shielding | Side shielding | Maximum ratio |
|---|---|---|---|---|
| 1 | None | None | None | 1.108 |
| 2 | 15 | None | None | 1.141 |
| 3 | 15 | Yes | Both sides and cover the whole autoclave, as shown in Figure 3.8 | 1.157 |
| 4 | 15 | Yes | Both sides and cover only half of the autoclave, as shown in Figure 3.9 | 1.168 |
| 5 | 30 | Yes | Both sides and cover only half of the autoclave, as shown in Figure 3.9 | 1.140 |

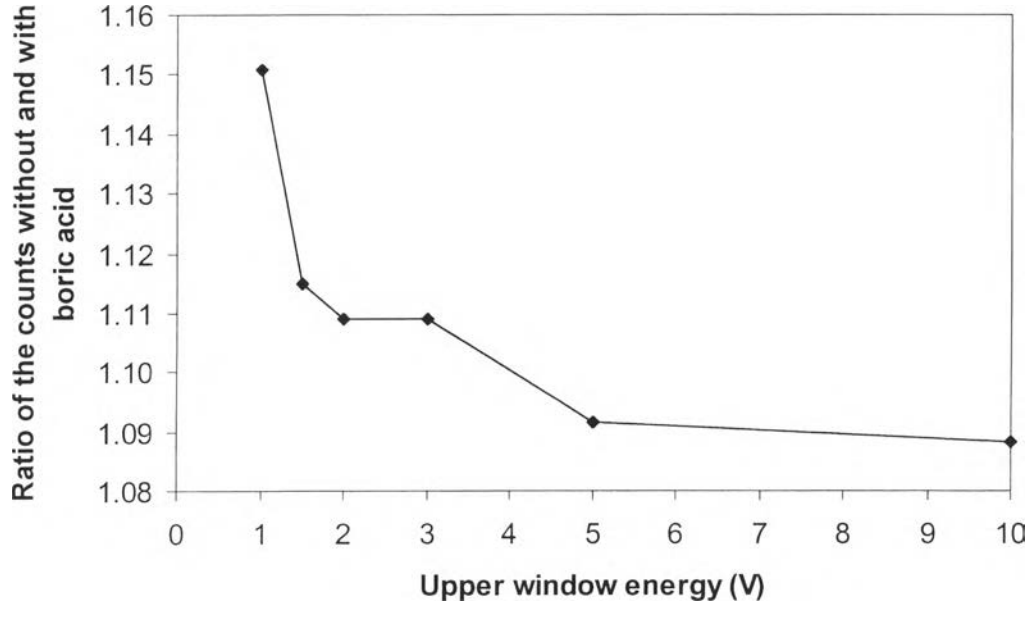


**Figure 4.27** Change in ratio of counts without and with boric acid as the upper window energy changes; lower window energy of 0.26 V, Gain 50 and 10-minute counting period.

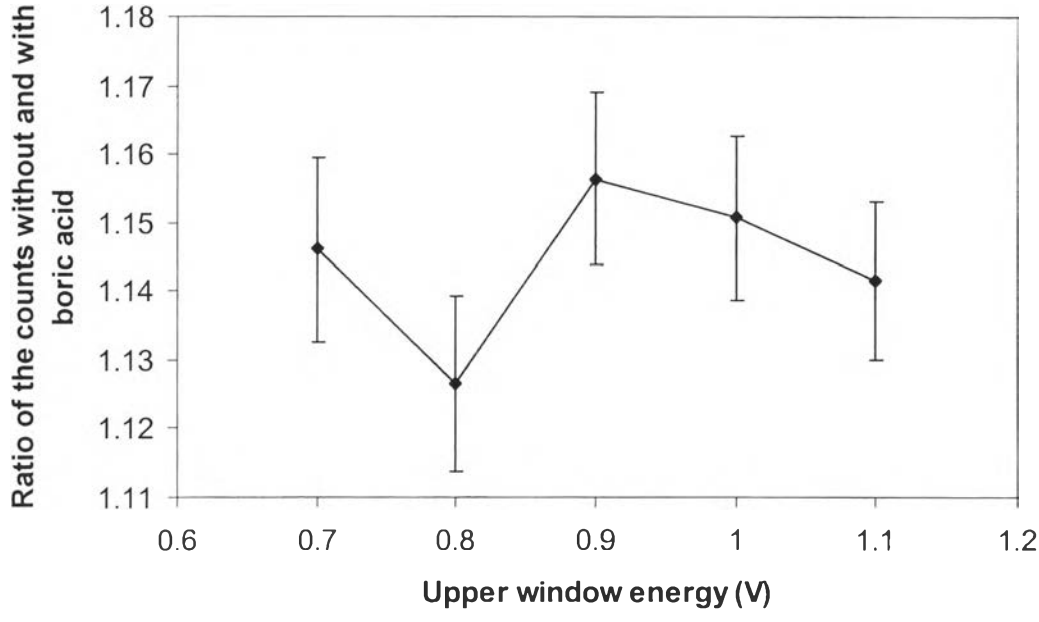


**Figure 4.28** Change in ratio of counts without and with boric acid as the upper window energy changes from 0.7 to 1.1 V; lower window energy of 0.26 V, Gain 50 and 10-minute counting period.

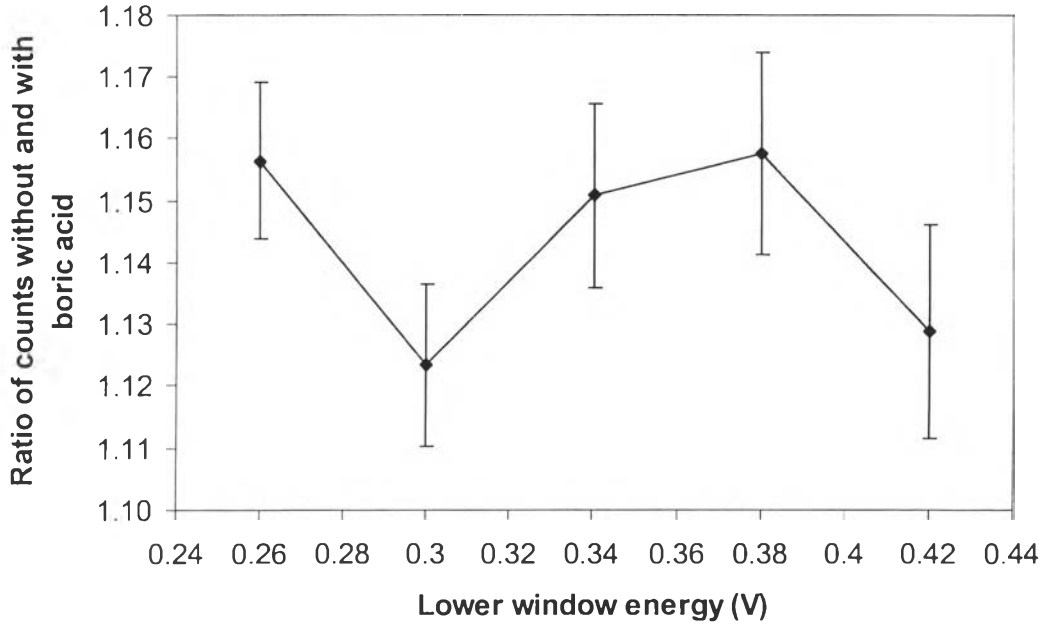


**Figure 4.29** Change in ratio of counts without and with boric acid as the lower window energy changes; upper window energy of 0.9 V, Gain 50 and 10-minute counting period.

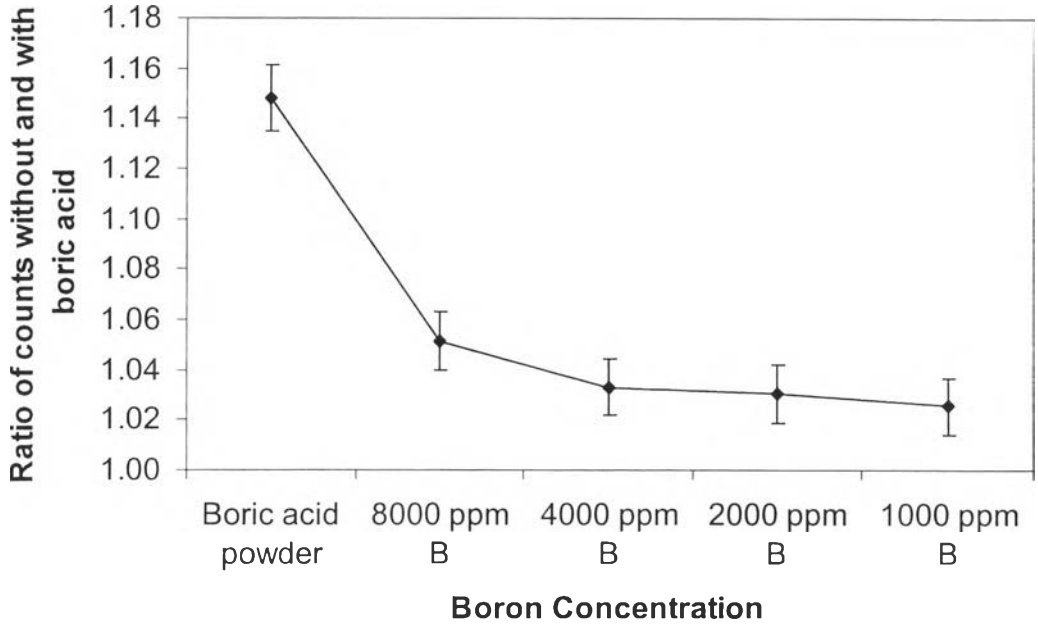


**Figure 4.30** Change in ratio of the counts without and with boric acid solution for various boron concentrations at Gain 50, 15-minute counting period at lower and upper window energies of 0.38 V and 0.9 V, respectively.

With the lower and upper window energies of 0.38 V and 0.9 V, respectively, the effects of various concentrations of boric acid solution inside the tube were investigated. As shown in Figure 4.30, the count ratio decreased dramatically as the boric acid was dissolved and diluted. The minimum distinguishable boron concentration was determined by statistical analysis. The count rate at the minimum boron concentration has to differ from that in the absence of boron by at least two standard deviations at a 95% confidence level. That is,

$$\overline{C}_0 - \overline{C}_{b,\min} \geq 2\overline{\sigma}_0 + 2\overline{\sigma}_b \qquad (4.2)$$

where $\overline{C}$ and $\overline{\sigma}$ are the mean count and standard deviation of mean, respectively, and the subscripts 0 and $b$ designate the condition without and with boron, respectively. The minimum $\overline{C}_b$ was calculated as shown in Appendix G. Table 4.9 shows a summary of the results.

**Table 4.9** Summary of neutron measurements

| Conditions | Ratio of the counts without and with boric acid obtained from experiments | Average count | Standard deviation | $\overline{C}_{b,\min}$ based on 95% confidence |
|---|---|---|---|---|
| Empty tube | - | 5462.33 | 42.67 | - |
| Boric acid powder | 1.148 | 4759 | 39.83 | 452.18 |
| 8000 ppm B | 1.051 | 5195.33 | 41.61 | 3523.85 |
| 4000 ppm B | 1.033 | 5287.33 | 41.98 | 8396.4 |
| 2000 ppm B | 1.030 | 5302 | 42.04 | 10039.71 |
| 1000 ppm B | 1.025 | 5326.67 | 42.14 | 14109.26 |

According to these results at a confidence level of 95%, the presence of boric acid powder and 8000 ppm B solution can be detected in a 15-minute counting period. For solutions below 4000 ppm B, the counts are too low. One can try to increase the counting period or use a stronger source to increase the counts. It should be noted that if the confidence level is changed, the minimum counts required are also changed.

The effect of the thermal neutron cloud created inside the autoclave on the counting efficiency was tested with a cadmium sheet, which has a neutron cut-off energy in the thermal energy range. The upper window energy was set at 0.9 V, based on previous results. The ratios of counts without and with the cadmium sheet in front of the detector with various lower window energies are shown in Figure 4.31. The best contrast was at a lower window of 0.42 V; however, it was almost the same as at 0.38 V. Hence, it can be concluded that the lower window energy was set at the optimum point, and this was confirmed with the cadmium sheet testing. Since cadmium is a stronger neutron absorber than boron, the ratio obtained from cadmium sheet testing was higher than that from boron testing.

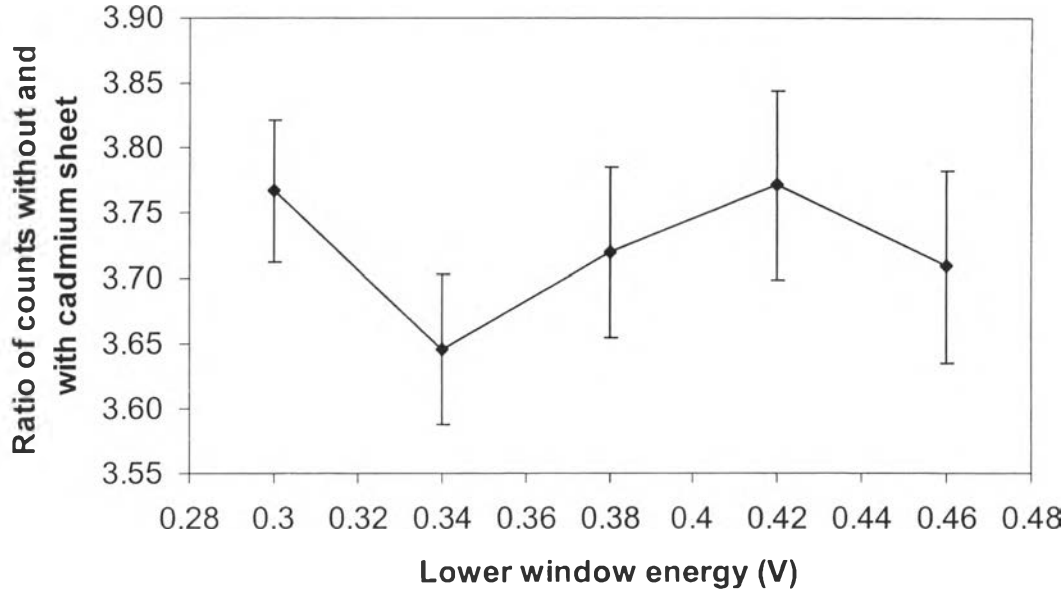


**Figure 4.31** Change in ratio of the counts without and with a cadmium sheet as the lower window energy changes; upper window energy of 0.9 V, Gain 50 and 15-minute counting period.

According to the MCA results with the He-3 detector, gamma-ray emission was one of the disturbances which affected the analysis. Hence, a $BF_3$ detector, which is less sensitive to gamma rays, was employed. The MCA pulse-height distribution from the $BF_3$ detector with and without boric acid is shown in Figure 4.32. In the $BF_3$ detector, two neutron reactions take place and both produce relatively high Q-values (the energy of particles and/or nuclei that causes ionization of a gas detector), in the MeV range, compared to the energy of slow neutrons, in the eV range (Hussein, 2003). The peaks on the right-hand side of the distribution were due to the neutron reactions. The few peaks on the left-hand side corresponded to noise and gamma rays and were ignored. The MCA result gave an estimation to set the lower and upper window energies for the SCA analysis in the next step. It should be noted that the number of pulses obtained from the $BF_3$ detector was much lower than the number from He-3, although the counting period was twice as long.

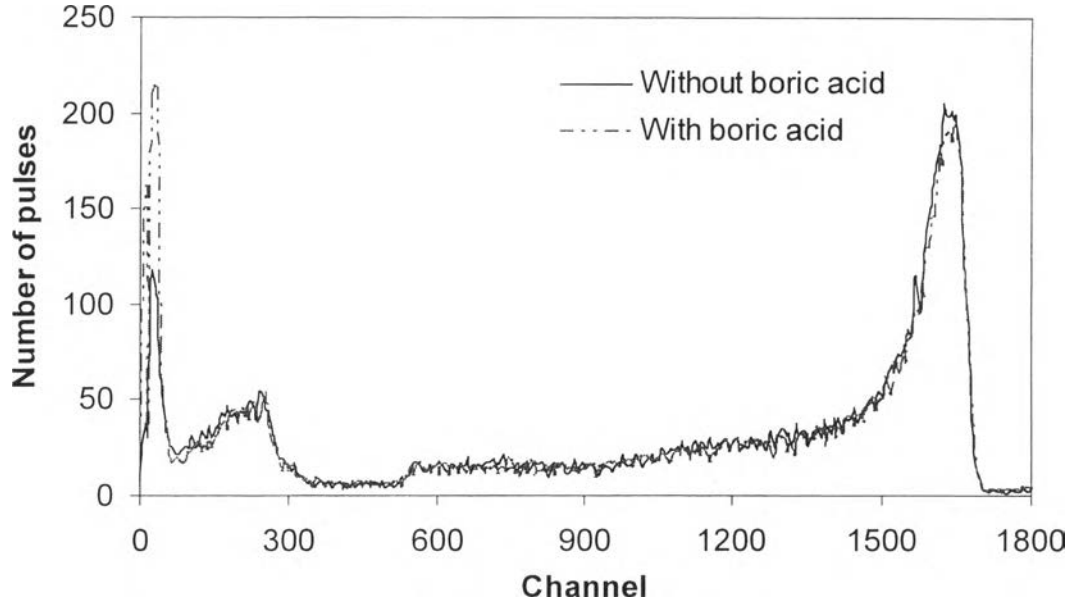


**Figure 4.32** Comparison of pulse-height distribution with and without boric acid; $BF_3$ detector, Gain 50 and one-hour counting period.

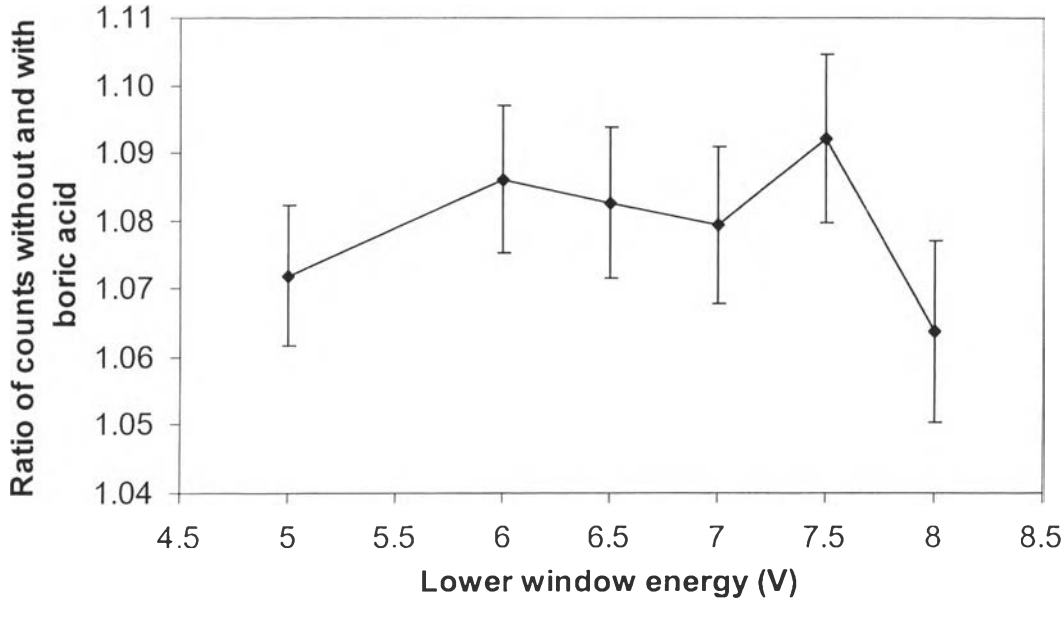


**Figure 4.33** Change in ratio of counts without and with boric acid as the lower window energy changes; $BF_3$ detector, upper window energy of 9 V, Gain 50 and one-hour counting period.

According to the MCA results, the signal almost disappeared depleted at about channel 1700, which was equivalent to the upper window energy of 9 V for the SCA. Since the region of interest with the MCA was at high channel number, the upper window energy for the SCA was set at 9 V, and the lower window energy was varied from 5 to 8 V.

As shown in Figure 4.33, the best contrast was obtained with a lower window energy of 7.5 V. Hence, the lower window energy was set at 7.5 V and the upper window energy was varied. Varying the upper window energy from 8.5 to 9.5 V did not affect the ratio of counts without and with boric acid, as shown in Figure 4.34. Therefore, with the upper window energy of 9 V, the lower window energy was varied to test the thermal neutron cloud generated inside the autoclave with a cadmium sheet.

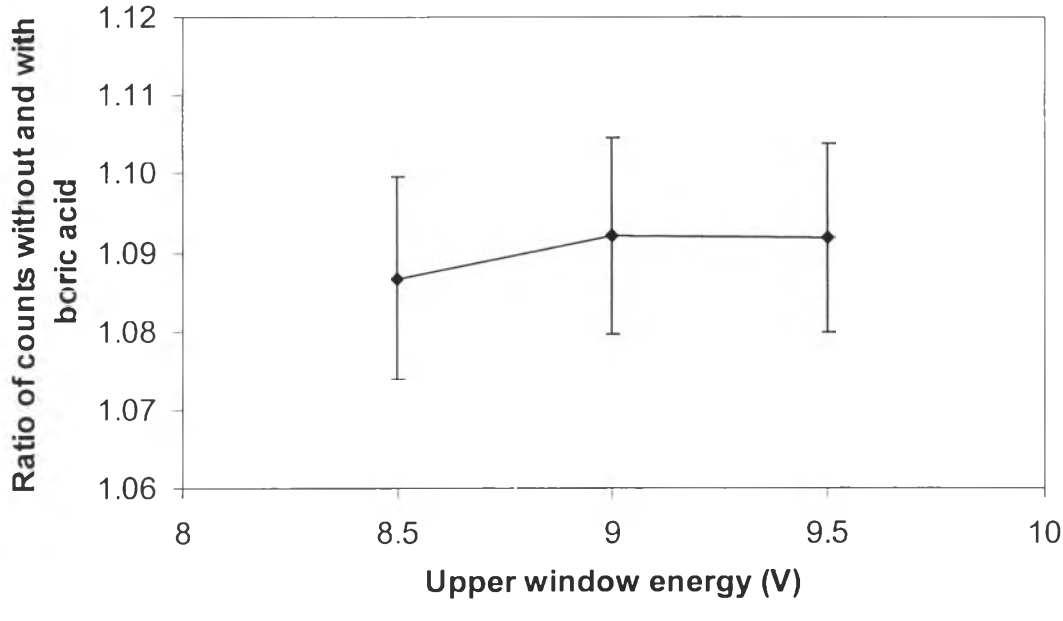


**Figure 4.34** Change in ratio of counts without and with boric acid as the upper window energy changes; $BF_3$ detector, lower window energy of 7.5 V, Gain 50 and one-hour counting period.

Figure 4.35 shows that the highest ratio of counts without and with the cadmium sheet was obtained at a lower window energy of 7 V. This means that the thermal neutron cloud was most effectively utilized when the lower and the upper

window energies were set at 7 and 9 V, respectively. This disagrees with the result in Figure 4.33. However, Figure 4.33 indicates that the ratios obtained with the lower window energies at 7 and 7.5 V were not much different. Therefore, it can be concluded that the best ratio of counts without and with boric acid powder in the tube in the middle of the autoclave obtained by $BF_3$ detector is 1.08; this was obtained with settings of the lower and the upper window energies of 7 and 9 V, respectively.

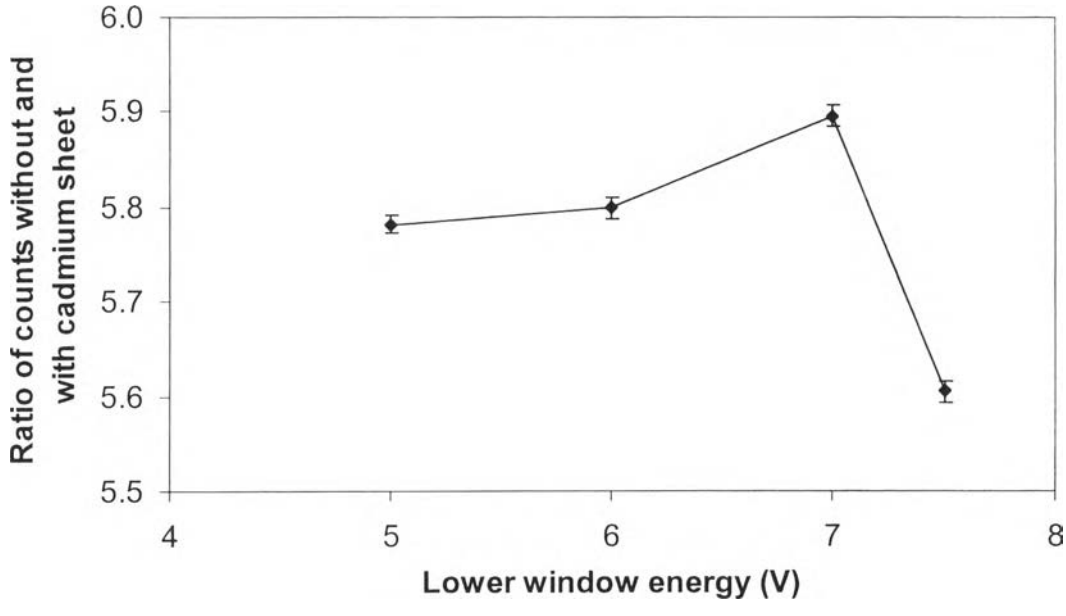


**Figure 4.35** Change in ratio of the counts without and with a cadmium sheet as the lower window energy changes; $BF_3$ detector, upper window energy of 9 V, Gain 50 and one-hour counting period.

The experiments indicate that the He-3 detector gives a better contrast than the $BF_3$ detector for detecting the presence of boron in the middle of the autoclave surrounded by a large volume of water. The He-3 detector also has a higher efficiency, which gives better in term of counting statistics. However, the efficiency of the $BF_3$ counter can be improved by increasing the gas pressure.

The use of cadmium sheet to test the thermal neutron cloud shows that the ratio of counts without and with cadmium from $BF_3$ detector was better than that of He-3 detector: 5.9 versus 3.75. This is different from the finding of the boric acid experiments. The reason is that He-3 has a higher cross-section and therefore can detect both thermal and fast neutrons. On the other hand, $BF_3$ detector is known

as thermal neutron detector because of a lower cross-section. Cadmium has a very high neutron cross-section at thermal energy, which means that it is opaque to thermal neutrons. With the use of a radioisotopic source associated with a moderating material, there were thermal and slowed-down neutrons present in the environment. A cadmium sheet in front of a detector is a barrier to thermal neutrons but not to slowed-down neutrons. Therefore, cadmium has more effect on a $BF_3$ detector than on a He-3 detector.

### 4.3.2 Prompt Gamma-Ray Activation Analysis

The results of the neutron flux depression experiment indicated that wax in front of the source and around the autoclave induces a thermal neutron cloud, which can induce extra absorption by the boron. Hence, in this experiment, a plate of 1.5 cm-thick wax was placed in front of the source and two bars of 4-cm thick wax were placed beside two sides of the autoclave, opposite to the source and the detector. Energy calibrations on the MCA were performed with two reference sources: Cs-137 and Co-60. Cesium-137 gives photons of energy 662 keV and Co-60 gives photons of energy 1773 and 1333 keV. With a high voltage power supply of 650 V and amplification at Gain 200, the MCA was calibrated.

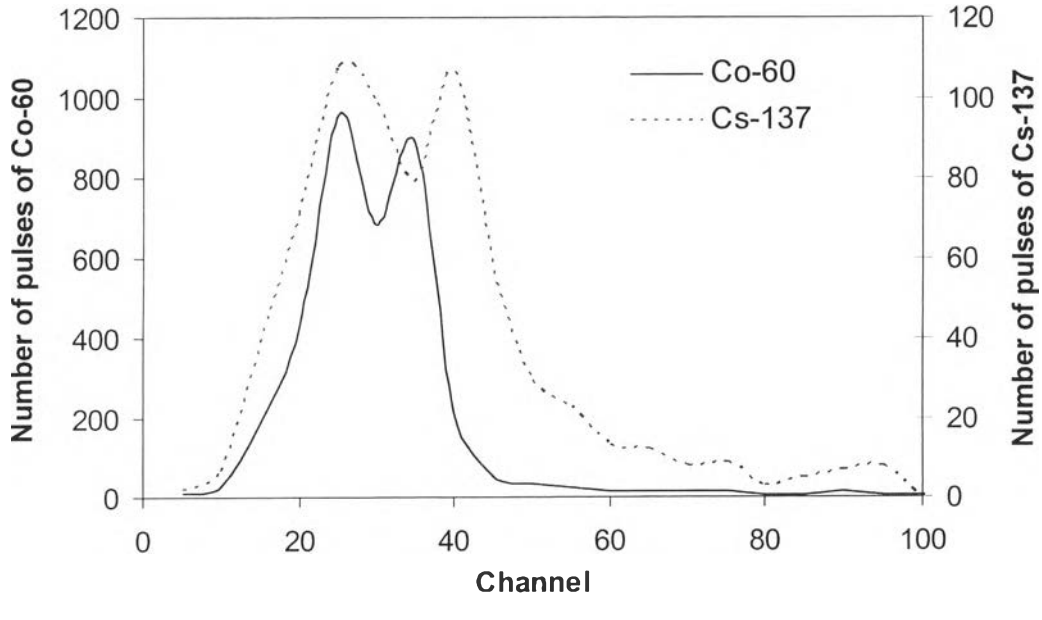


**Figure 4.36** Pulse-height distribution on calibration sources; Gain 200 and 650 V power supply.

In Figure 4.36, there are two dominant peaks for Cs-137, and they overlap the peaks of Co-60. Cesium-137 should give one dominant peak, which should be separate from the Co-60 peaks. The amplification was probably too low; therefore, the signals were packed in a small region and could not be distinguished. Higher amplification, Gain 500, was tried; the results are shown in Figure 4.37.

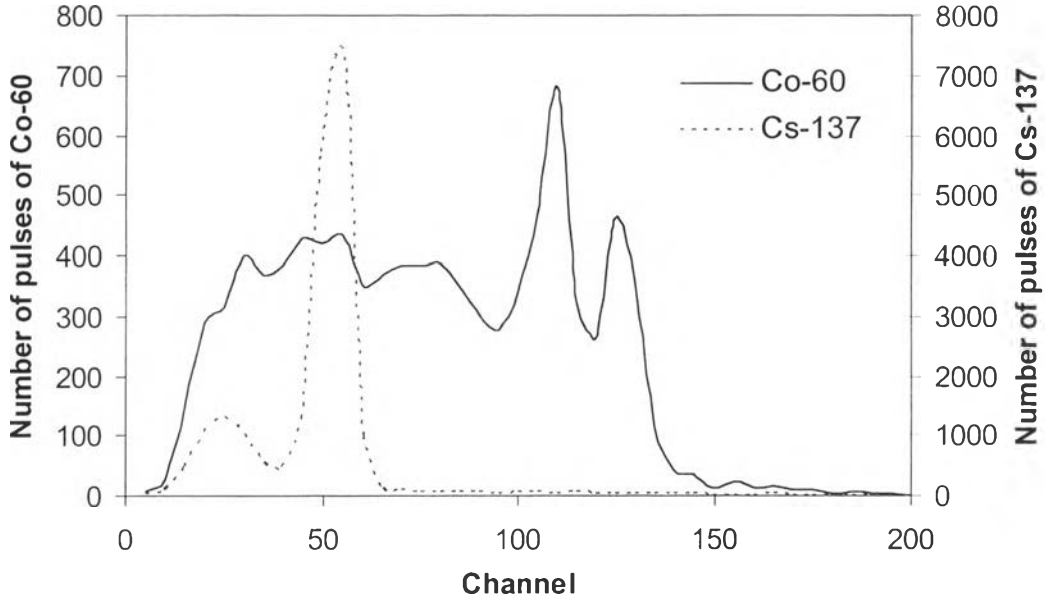


**Figure 4.37** Pulse-height distribution on calibration sources; Gain 500 and 650 V power supply.

Figure 4.37 shows clear, distinct peaks. The channels of the peaks were plotted versus energy and a linear calibration was obtained – as depicted in Figure 4.38. Two more calibrations were done at Gain 100 and 200 with 1000 V power supply. In further MCA analysis, the pulse-height distribution was plotted against energy. The energy of 478 keV is of interest since it is the gammy-ray energy produced by neutron absorption.

The tube with and without boric acid powder was inserted in the middle of the autoclave and analyzed by the MCA a with 30-minute counting period and different amplifications: Gain 500 at 605 V, and Gain 100 and 200 at 1000 V. The results are shown in Figures 4.39 through 4.41.

Figures 4.39 to 4.41 show that the amplification that gave the best contrast is Gain 500 with 650 V high voltage power supply. The ratio of counts with and without boric acid at such setting was 1.05.

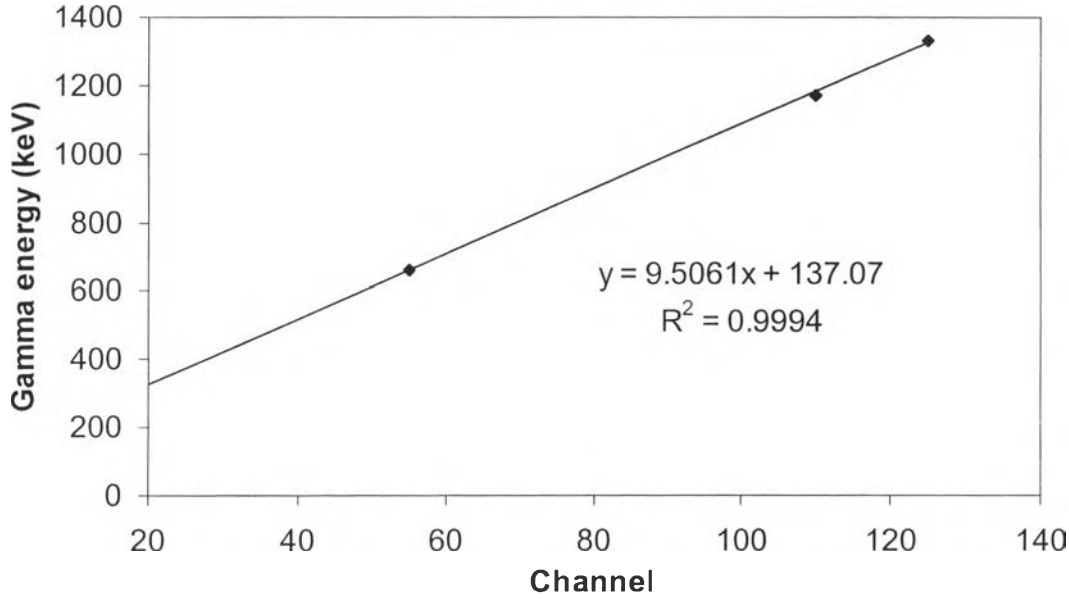


**Figure 4.38** Calibration curve; Gain 500 and 650 V power supply.

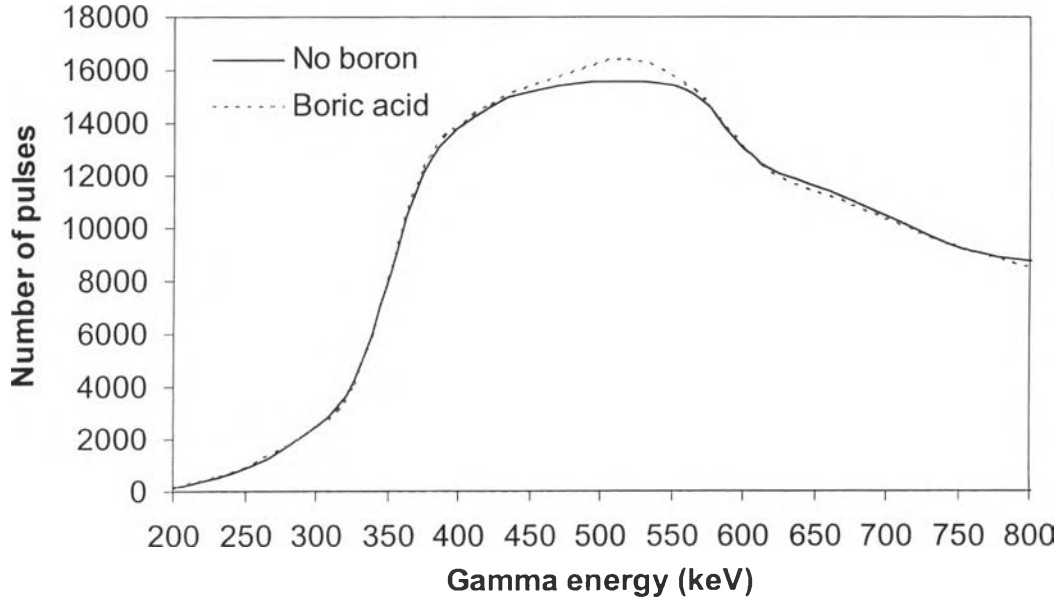


**Figure 4.39** Pulse-height distribution for gamma rays with and without boric acid; Gain 500, 650 V power supply and 30-minute counting period.

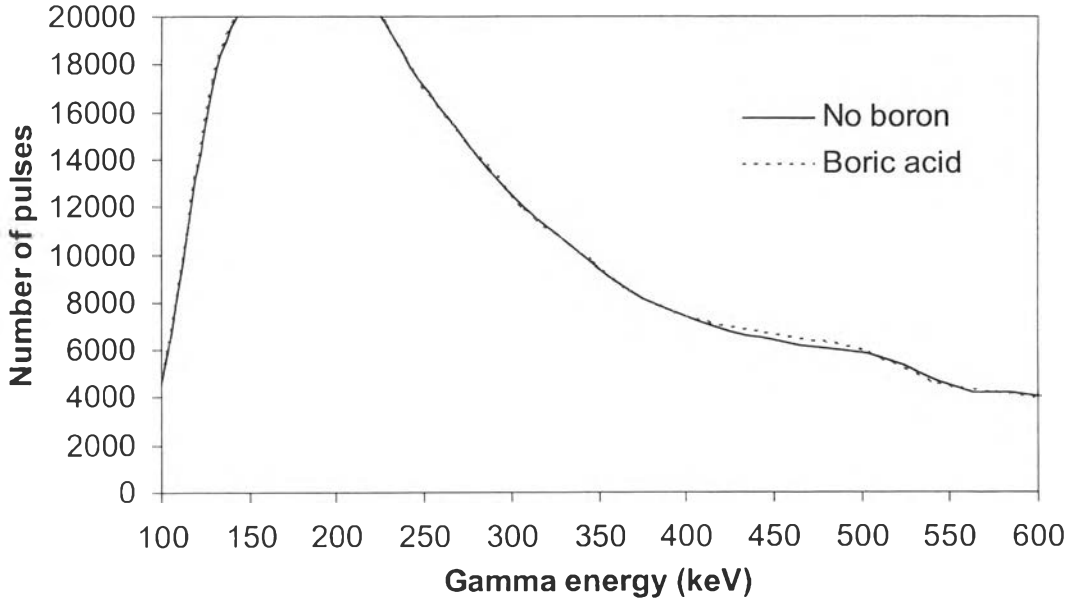


**Figure 4.40** Pulse-height distribution for gamma rays with and without boric acid; Gain 100, 1000 V power supply and 30-minute counting period.

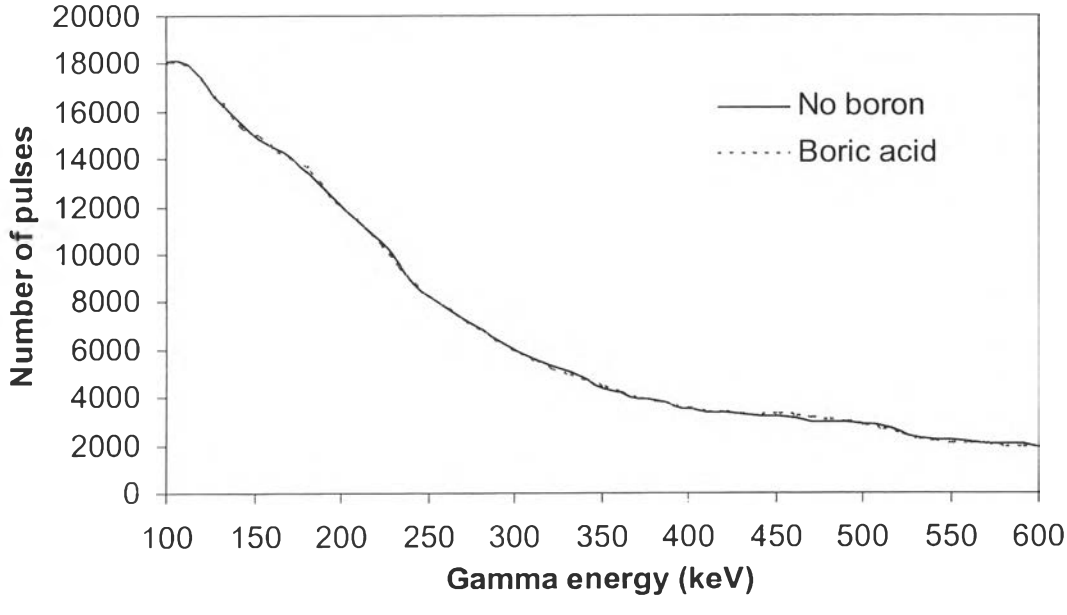


**Figure 4.41** Pulse-height distribution for gamma rays with and without boric acid; Gain 200, 1000 V power supply and 30-minute counting period.

Another two different arrangements were tested to see if the positioning of lead bricks improved the contrast. Figures 4.42 and 4.43 show the

pulse-height distributions when a lead brick was placed besides the source and when there was no brick, respectively. From Figure 4.42, counts without and with boron are similar, with minor discrimination amounting to a ratio of 1.02 at 478 keV. When there was no brick, and the detector was fully exposed to the source, the number of pulses doubled, as shown in Figure 4.43. No significant discrimination between counts without boron and counts with boron is evident. This means that the source contributed too many photons, which disturbed the analysis.

The total cross-section of $^{10}B$ at thermal energy is 3840 barns; 3837 barns contribute to a (n,α) reaction that emits a prompt gamma ray at energy of 478 keV. Regardless of noise that might interrupt the analysis and affect the efficiency of the detectors, the two methods, neutron slowing-down followed by absorption and Prompt Gamma-Ray Activation Analysis (PGAA), should have given the same result. However, the results obtained from PGAA experiment were not as good as those obtained from neutron slowing-down followed by absorption experiment. This can be explained by the fact that in the setup there were two major ways that the interfering photons could be generated: scattering and activation. The neutron source itself released photons, which were scattered towards the detector and interfered with the analysis. Also, during neutron irradiation, hydrogen in the water and nickel in the autoclave material produced photons of energy 2223 keV and 465 keV, respectively (Baechler *et al.*, 2002; Magara and Yonezawa, 1998). Although hydrogen gives a very different photon energy from that of $^{10}B$, such photon energy is altered by scattering. This results in a wide background photo spectrum, above which the 478 keV photon from the $^{10}B$ (n,α) reaction resides. The amount of inspected sample is also important, and since photon energy released by nickel is close to that released by boron, their signals would interfere with each other. To estimate which reaction contributed more signals, the total interaction rates based on the amounts and cross sections of nickel and boron were calculated and compared (see Appendix H). The calculation showed that total interaction rate of boron was about four times higher than that of nickel. This means that signals with and without boron can be observed as shown in Figure 4.39. Nevertheless the difference was too small to be useful.

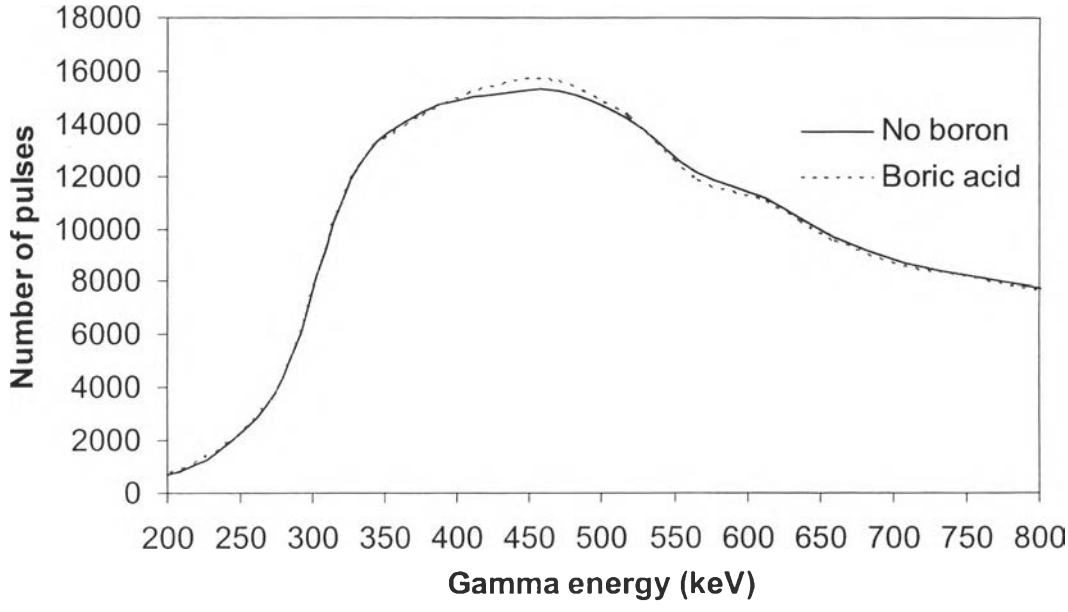


**Figure 4.42** Pulse-height distribution for gamma rays with and without boric acid; lead brick besides the source, Gain 500, 650 V power supply and 30-minute counting period.

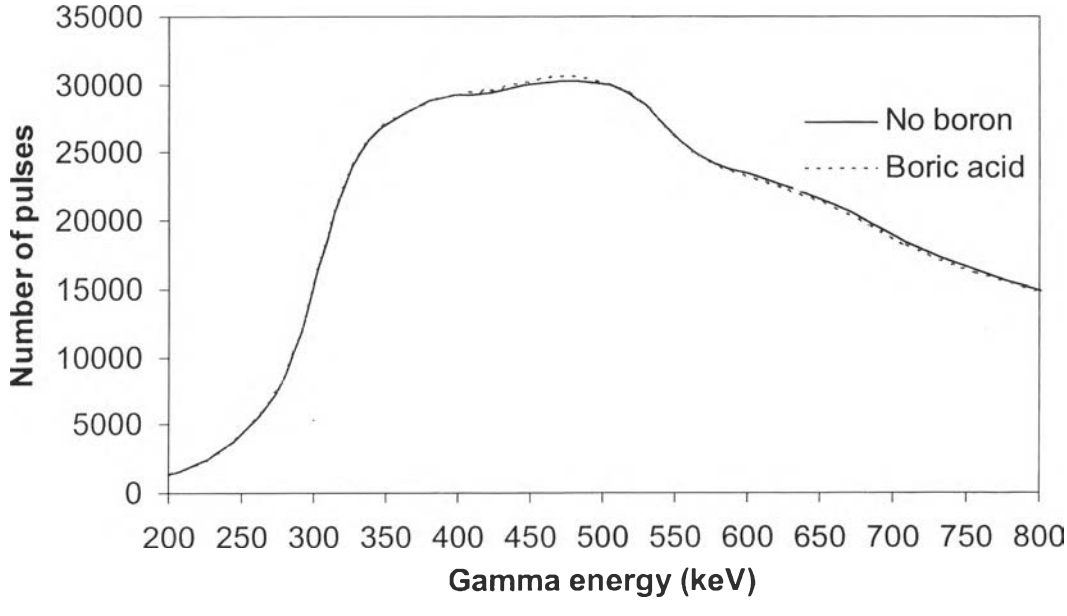


**Figure 4.43** Pulse-height distribution for gamma rays with and without boric acid; no lead brick, Gain 500, 650 V power supply and 30-minute counting period.